Energy Storage Materials 25 (2020) 382–403

Contents lists available at ScienceDirect

Energy Storage Materials

journal homepage: www.elsevier.com/locate/ensm

Recent nanosheet-based materials for monovalent and multivalent ions storage

Nan Li [a,b,c,1], Xin Xu [a,b,1], Bowen Sun [b], Keyu Xie [c], Wei Huang [a,d,**], Ting Yu [b,*]

[a] Shaanxi Institute of Flexible Electronics (SIFE), Northwestern Polytechnical University (NPU), Xi'an, 710072, China
[b] Division of Physics and Applied Physics School of Physical and Mathematical Sciences, Nanyang Technological University, 637371, Singapore
[c] State Key Laboratory of Solidification Processing, Center for Nano Energy Materials, School of Materials Science and Engineering, Northwestern Polytechnical University and Shaanxi Joint Laboratory of Graphene (NPU), Xi'an, 710072, China
[d] Key Laboratory of Flexible Electronics (KLOFE) & Institute of Advanced Materials (IAM), Nanjing Tech University (NanjingTech), Nanjing, 211800, China

ARTICLE INFO

Keywords:
Nanosheet-based electrode materials
Monovalent ion batteries
Multivalent ion batteries

ABSTRACT

Owing to the unique advantages of short solid-state diffusion length for metal ions, outstanding ability to alleviate the huge volume expansion of the electrode during repeated charge/discharge process, considerable large amount of channels for electrolyte access leading promoting fast ion diffusion between electrode, and numerous exposed active sites, nanosheet structures are regarded as the ideal electrode structures for achieving high capacity and ultrafast charge/discharge of energy storage. Herein, this review provides a comprehensive introduction of recent nanosheet-based electrode materials for high performance batteries, like monovalent ion (lithium and sodium) batteries and multivalent ion (magnesium, zinc and aluminum) batteries. Facile and simple strategies of synthesizing electrodes and different mechanisms of energy storage are presented. Furthermore, the challenges and development directions of nanosheet-based materials and rechargeable battery systems are discussed.

1. Introduction

The ever-fast fossil fuel consumptions in our daily lives have led to the environmental pollution and energy depletion [1]. Therefore, people are looking for new opportunities from renewable resources, such as solar and wind, which are considered as the clean and environmental friendly energy. Unfortunately, these energies are inherently unstable and cannot be utilized directly as power sources in energy storage and conversion applications [2]. Electrochemical energy storage and innovative materials chemistry are regarded as the key point of achieving energy storage and conversion with high efficiency and gainful convenience [3]. As a result, the further development of the rechargeable battery systems, such as monovalent ion (lithium and sodium) batteries (denoted as LIBs, SIBs) and multivalent ion (magnesium, zinc and aluminum) batteries (denoted as MIBs, ZIBs, AIBs), has attracted intensive attention.

The realization of high-power capability is known to be the most important factor to achieve high power density applications, like electric vehicles and portable electronic devices. However, the sluggish kinetic issues incorporating tardy ion/electron diffusion in electrochemically active electrodes have greatly impeded the achievement of high-rate capability. It is well known that the characteristic time constant t for ions diffusion is proportional to the square of the diffusion length L ($t \approx L^2/D$) [4,5]. Based on this formula, an effective strategy has been proposed by decreasing the multi-scale dimensions of the electrode materials, which hold the potential to shorten ion and electron transport lengths and improve current rates [6,7]. Therefore, various nanoscale materials were fabricated and employed as promising electrodes for energy storage applications, such as nanotubes [8], nanoparticles [9], nanobelts [10], nanowires [11], and nanosheets [12,13]. Among these different nanostructures, nanosheets have attracted intensive attention due to the following advantages. Compared with nanoparticles, nanosheets possess considerable surfaces and channels for electrolyte access, resulting in promoting fast ion transportation between the battery electrodes. Compared with nanowires and nanotubes, nanosheets possess the enhanced conductivity within a two-dimensional plane, which is favorable for ion migration and diffusion. Compared with nanobelts, nanosheets own relatively more exposed active sites due to their ultrathin architectures [14], which is advantageous for enhancing the ion storage

* Corresponding author.
** Corresponding author. Shaanxi Institute of Flexible Electronics (SIFE), Northwestern Polytechnical University (NPU), Xi'an, 710072, China.
E-mail addresses: iamwhuang@nwpu.edu.cn (W. Huang), yuting@ntu.edu.sg (T. Yu).
[1] These authors contributed equally to this work.

https://doi.org/10.1016/j.ensm.2019.10.002
Received 1 August 2019; Received in revised form 26 September 2019; Accepted 2 October 2019
Available online 5 October 2019
2405-8297/© 2019 Published by Elsevier B.V.

performances. All of the advantages promise nanosheet-based materials an ideal electrode material for storing various metal ions and achieving high-capacity and rate energy storage.

Nanosheet is a two-dimensional (2D) nanostructure with thickness in a scale ranging from 1 to 100 nm. A typical example of a nanosheet is graphene, which consists of a single layer of carbon atoms with hexagonal lattices. To our best knowledge, different kinds of layered titanates, such as $H_2Ti_3O_7$, $H_2Ti_4O_9 \cdot 1.2H_2O$ and $H_2Ti_5O_{11} \cdot 3H_2O$, have been synthesized in the 1990s, which are the earliest reported nanosheet-based materials [15]. After that, various kinds of nanosheets have been prepared, such as metal oxides and metal chalcogenides. The morphologies of these materials have been developed in recent years, what's more, various strategies such as inducing defects, constructing heterostructures, as well as doping, have been employed to improve the electrochemical performances of batteries. Recent electrodes constructed by nanosheet-based materials for high performance batteries may be classified into three major species, transition metal oxides (TMOs) [16], transition metal chalcogenides (TMCs) [17], and other type nanosheets, like MXene [18], carbon nanosheets [19] and porous graphene [20–22] (Fig. 1). TMOs, such as MnO_2 [23], TiO_2 [24–26], ZnO_2 [27], MoO_2 [28], NiO [29] and Co_3O_4 [30], which composed of the transition metal element from the d-block of the periodic table with oxygen element. Owing to the abundant natural reserve, special redox chemistry mechanisms, variable bonding structure, unobstructed ion transfer channels, as well as interactions with short distance between ions and charge carriers [16,31], TMOs hold the promising potential in rechargeable batteries. In addition, layered TMOs with stacked 2D sheets possess strong in-plane covalent interactions and weak van der Waals (vdWs) interactions [32]. Due to the improved electrochemical properties of 2D form layered TMOs compared to the bulk counterpart, achieving effective exfoliation is the key point for applying TMOs as electrode materials in rechargeable battery systems. 2D layered TMCs composed of groups IV−X transition metals with chalcogen display unique physical and chemical property [33]. Like the structure of graphene, a metal center is bonded by other surround six chalcogen atoms within each layer and every single layer is coupled through vdWs interactions [34], thus, single- or few-layer TMCs sheets can be easily exfoliated from bulk materials. Merits in high specific surface area, abundant exposed atoms, as well as unsaturated coordination at edge, TMCs hold a great potential in electrochemical energy storage field, since electrochemical reactions usually occur at surfaces or interfaces [35]. Recently, 2D MXene [36], layered phosphides [37], as well as porous graphene nanosheets [38–40] were also explored for electrode materials in rechargeable batteries.

Herein, this review provides a comprehensive introduction of recent nanosheet-based electrode materials for high performance batteries, like LIBs, SIBs, MIBs, ZIBs, AIBs. Various facile and simple synthesis strategies, such as hydrothermal [41], microwave-assisted [42], low temperature synthesis [43], thermal decomposition [44], as well as precipitation process [45] are presented. The different mechanisms of energy storage are discussed in the meantime. Moreover, taking advantage of crystal geometry control, alloying, defect engineering, doping, as well as heterostructure configuration is critical to adjust the properties of these nanosheet-based materials to extend the range of their practical availability [35,46].

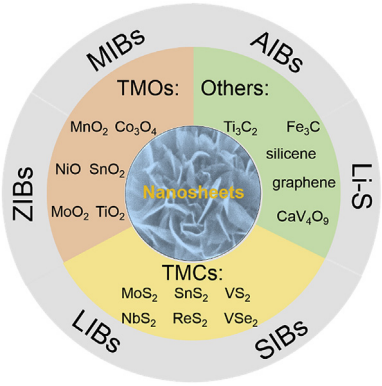

Fig. 1. Nanosheet-based materials for different kinds of batteries.

2. Nanosheet-based materials for LIBs

Although LIBs have achieved broad success in commercial market on account of the energy density consideration, the weak point of fail in fast charging/discharging has hindered their further applications in high power density fields [47–51]. To solve this problem, recently, numerous nanosheet-based materials have been successfully designed and prepared for further enhancing the rapid Li^+ storage properties. As can be seen from Table 1, the common employed materials are mainly MnO_2, Co_3O_4, MoO_2, NiO, TiO_2, SnO_2, MoS_2, SnS_2, VS_2, NbS_2, ReS_2, VSe_2, Ti_3C_2, graphene, CaV_4O_9, and silicene, etc. It's worth noting that most of these materials exhibit a high initial capacity of over 1000 mA h g^{-1}, while the Coulombic efficiency of the 1st cycle is not ideal.

2.1. TMOs nanosheets

Among the numerous TMOs, manganese dioxide (MnO_2) holds promising potential for LIB anode applications because of the high theoretical capacity (1233 mA h g^{-1}), wide potential window, abundant natural reserve, and non-toxic [52–54]. Xiong and co-workers synthesized the genuine unilamellar MnO_2/graphene superlattice nanostructure through molecular-scale hybridized strategy, which can shorten diffusion lengths, expose more active sites, reduce volume changes, and thus lead to further improvements of electrochemical performance [55]. Two-step conversion reaction, confined in the 2D channels between the graphene networks, is proposed as the mechanism of Li storage (Fig. 2a). First step, MnO_2 nanosheets are converted into MnO sheets at approximately 0.7 V, and followed by converted into Mn layers at about 0.1 V at the second step [56]. The high-resolution TEM (HRTEM) confirmed the lithiation mechanism. Before lithiation, MnO_2 and rGO with spacings of ~0.8 and 1.4 nm, respectively, can be found (Fig. 2b). After one step lithiation, the lattice spacings changes to ~0.27 nm (Fig. 2c), which indicates the {111} planes of MnO layer. After lithiation completed, the {111} lattice planes of Mn^0 with lattice spacing of ~0.22 nm are mainly observed (Fig. 2d), which indicates MnO are reduced to Mn layer.

As another important kind of TMOs materials, cobalt tetroxide (Co_3O_4), which can store eight lithium atoms per formula unit, has been extensively investigated due to the excellent physical properties, as well as its high theoretical capacity (890 mA h g^{-1}) [30,57]. Yan and co-workers prepared the stacked ultrathin Co_3O_4 nanosheets with surface anion functionalization (Fig. 2e) [58]. Such structure possesses abundant interconnected channels with negative surface charge, which is beneficial for fast Li^+ transport. The mechanism of Li^+ storage in Co_3O_4 nanosheets was revealed by CV curves (Fig. 2f). During the 1st cycle, a cathodic peak at 0.69 V represents the reduction process from Co_3O_4 to Co, and the formation of Li_2O, together with the formation of solid electrolyte interphase (SEI). On the other hand, the charge peak at 2.08 V signifying the oxidation process from Co to Co_3O_4. During the next cycles, except for the discharge peak shifted from 0.69 V to a higher voltage of 0.98 V, the other peaks coincided well with the first scan, which indicates high electrochemical reaction reversibility of the Co_3O_4 architecture. Although Co_3O_4 holds high specific capacity, poor electrical conductivity and high volume change (249%) have impeded the wide applications. Song and co-workers designed $ZnCo_2O_4$ doped Co_3O_4 hollow nanospheres [59], which can effectively relieve the volume expansion, thus exhibits high specific capacity (890 mA h g^{-1}) at high current density of 1 A g^{-1}.

Except for doping, forming porous structures is another effective way to enhance electrochemical performances. Co_3O_4 nanosheets with controllable pore size were fabricated by Chen and co-workers via a

Table 1
Summary of synthesis methods and electrochemical properties of various kinds of nanosheets for LIBs.

Materials	Synthesis method	Electrochemical performance				Ref.
		Coulombic efficiency	Initial capacity	Rate capability	Cycling stability	
MnO_2	solution-phase electrostatic assembly	54% (1st)	1395 mA h g^{-1} (0.1 A g^{-1})	545 mA h g^{-1} (6.4 A g^{-1})	480 mA h g^{-1} (5000th cycle at 5 A g^{-1})	[55]
Co_3O_4	liquid-phase reaction and post-annealing	70% (1st)	1145 mA h g^{-1} (1 A g^{-1})	137 mA h g^{-1} (20 A g^{-1})	375 mA h g^{-1} (1500th cycle at 5 A g^{-1})	[58]
MoO_2	sol-gel method and post-annealing	60% (1st)	967 mA h g^{-1} (0.1 A g^{-1})	341 mA h g^{-1} (5 A g^{-1})	300 mA h g^{-1} (1000th cycle at 10 A g^{-1})	[65]
NiO	precipitation and post-annealing	67% (1st)	1013 mA h g^{-1} (0.2 A g^{-1})	680 mA h g^{-1} (1.6 A g^{-1})	950 mA h g^{-1} (150th cycle at 0.2 A g^{-1})	[69]
TiO_2	solvothermal method	83% (1st)	240 mA h g^{-1} (335 mA g^{-1})	130 mA h g^{-1} (20C)	160 mA h g^{-1} (400th cycle at 5C)	[74]
SnO_2	hydrothermal and post-annealing	85.9% (1st)	1076 mA h g^{-1} (50 mA g^{-1})	656.2 mA h g^{-1} (1.5 A g^{-1})	471.2 mA h g^{-1} (1500th cycle at 0.9 A g^{-1})	[76]
MoS_2	hydrothermal and post-annealing	73% (1st)	1036 mA h g^{-1} (0.1 A g^{-1})	747 mA h g^{-1} (5 A g^{-1})	753 mA h g^{-1} (1000th cycle at 2 A g^{-1})	[86]
SnS_2	solvothermal method	80% (1st)	1200 mA h g^{-1} (0.2 A g^{-1})	620 mA h g^{-1} (10 A g^{-1})	1100 mA h g^{-1} (50th cycle at 0.2 A g^{-1})	[78]
VS_2	solvothermal method	–	1050 mA h g^{-1} (0.1 A g^{-1})	570 mA h g^{-1} (10 A g^{-1})	850 mA h g^{-1} (500th cycle at 1 A g^{-1})	[93]
NbS_2	oil-phase synthetic process	65.4% (1st)	924 mA h g^{-1} (0.1 A g^{-1})	461.3 mA h g^{-1} (10 A g^{-1})	612 mA h g^{-1} (1500th cycle at 3 A g^{-1})	[96]
ReS_2	electrospinning and hydrothermal	73.9% (1st)	630 mA h g^{-1} (0.1 A g^{-1})	360 mA h g^{-1} (2 A g^{-1})	440 mA h g^{-1} (400th cycle at 0.1 A g^{-1})	[100]
VSe_2	solvothermal method	76% (1st)	745 mA h g^{-1} (0.1 A g^{-1})	571 mA h g^{-1} (2 A g^{-1})	766 mA h g^{-1} (50th cycle at 0.1 A g^{-1})	[104]
Ti_3C_2	etching and sonication	42% (1st)	1730 mA h g^{-1} (0.1 A g^{-1})	167 mA h g^{-1} (2 A g^{-1})	828 mA h g^{-1} (100th cycle at 0.1 A g^{-1})	[109]
N-doped graphene	supramolecular polymerization and annealing	55.3% (1st)	1440 mA h g^{-1} (0.2C)	356 mA h g^{-1} (10C)	900 mA h g^{-1} (150th cycle at 0.2C)	[111]
CaV_4O_9	hydrothermal and post-annealing	73.5% (1st)	700 mA h g^{-1} (0.1 A g^{-1})	330 mA h g^{-1} (5 A g^{-1})	456 mA h g^{-1} (400th cycle at 0.5 A g^{-1})	[123]
Silicene	liquid oxidation and exfoliation	61.6% (1st)	870 mA h g^{-1} (0.1 A g^{-1})	312 mA h g^{-1} (5 A g^{-1})	721 mA h g^{-1} (100th cycle at 0.1 A g^{-1})	[127]

graphene oxide template-directed strategy [60]. The unique structure of porous Co_3O_4 nanosheets possesses the following three advantages, thus, holds great potential to achieve both excellent rate capability and high specific capacity. First of all, the hindered of electrode pulverization and promoted specific surface area can be achieved due to the highly interconnected Co_3O_4 and the porous framework, respectively [61]. In addition, the conductivity of electrodes can be increased efficiently owing to the continuous transport paths of electrons provided by this 2D porous structure, which beneficial to the fast charging/discharging [62]. Furthermore, the efficient Li^+ transport throughout the entire electrode can be achieved because the hierarchical porous architecture can obstruct the restack of nanosheets effectively, thus facilitate the transport of electrolyte ions. As a result, together with the above-mentioned superiorities, the 2D porous Co_3O_4 nanosheets can realize the superb rate capacity.

Molybdenum dioxide (MoO_2), as one kind of TMOs, possesses the advantages of high theoretical capacity, metallic characteristics of about 200 S cm^{-1} conductivity, low cost, and environment friendliness, therefore attracts widespread attention [63,64]. Zhao and co-workers synthesized the MoO_2 nanosheets, which are homogeneously dispersed in carbon nanosheets and together constructed tubular hierarchical structure, via a simple sol-gel approach and subsequently annealing process [65]. The distinct structure of as-prepared hierarchical MoO_2 tubes can not only facilitate the rapid diffusion of Li^+, but accommodate the mechanical stress along with the cycling charge-discharge processes as well. Moreover, the electrode resistance can be greatly reduced because of the existence of high electronic conductive MoO_2. What's more, the rate capability can be further improved due to the three-dimensional pathways of the Li^+ and electrolyte provided by cavities of tubular nanostructures (Fig. 2g). As a result, the hierarchical structure exhibits satisfactory electrochemical performances for Li^+ storage capability (~300 mA h g^{-1}), and maintain 89% capacity at 10 A g^{-1} after 10,000 cycles. The hierarchical tubular nanostructure can be preserved, which displays an excellent stability. CVs were conducted to further investigate the Li^+ storage (Fig. 2h). A wide reduction peak appears in the 1st cycle at ca. 1.27 V, which can be classified as the Li^+ insertion into the anode, and the following peak (ca. 0.67 V) is ascribed to the next conversion process from MoO_2 nanoclusters to Mo and Li_2O, as well as the appearance of SEI [66]. During the followed two circles, cathodic peaks at ca. 1.56 and 1.33 V can be attributed to the appearance of Li_xMoO_2 ($0 < x < 0.98$) due to the reversible Li^+ intercalation, and the other peaks at ca. 1.39 and 1.69 V can be attributed to Li^+ deintercalation [65]. The reversible phase transition of hierarchical tubular MoO_2 nanostructures between monoclinic MoO_2 and orthorhombic Li_xMoO_2 guarantees high electrochemical reaction reversibility of the electrode, which is revealed by the overlapping cycling CV curves.

Because of the thermal stability, physical and chemical stability, natural abundance and high theoretical capacity (718 mA h g^{-1}), nickelous oxide (NiO) is often investigated as another promising anode material for LIBs [67,68]. Hybrid nanostructures of NiO nanosheets anchored on carbon hollow spheres (NiO NSs@C) was prepared by Liang and co-workers via a facile precipitation reaction and thermal treatment subsequently (Fig. 2i) [69]. The structural characteristics of bowl-like and hierarchical features of NiO NSs@C particles can be obtained after annealing process (Fig. 2j). Moreover, the inset TEM image exhibits the hollow nanostructures which agrees well with Fig. 2j. So as to further explore the mechanism Li^+ storage mechanism, CV was performed between the potential window of 0.005–3.0 V (Fig. 2k). In the first cathodic scan, an obvious current peak occurring at ca. 0.5 V is regarded as the formation of SEI as well as the reduction reaction of NiO [70]. The anodic peak occurring at about 1.46 V and 2.2 V can be attributed to the oxidation of Ni and the partial SEI film decomposition, respectively [71]. Furthermore, the maintained cycling of CV curves demonstrating the good electrochemical reversibility of NiO NSs@C hybrid nanostructures.

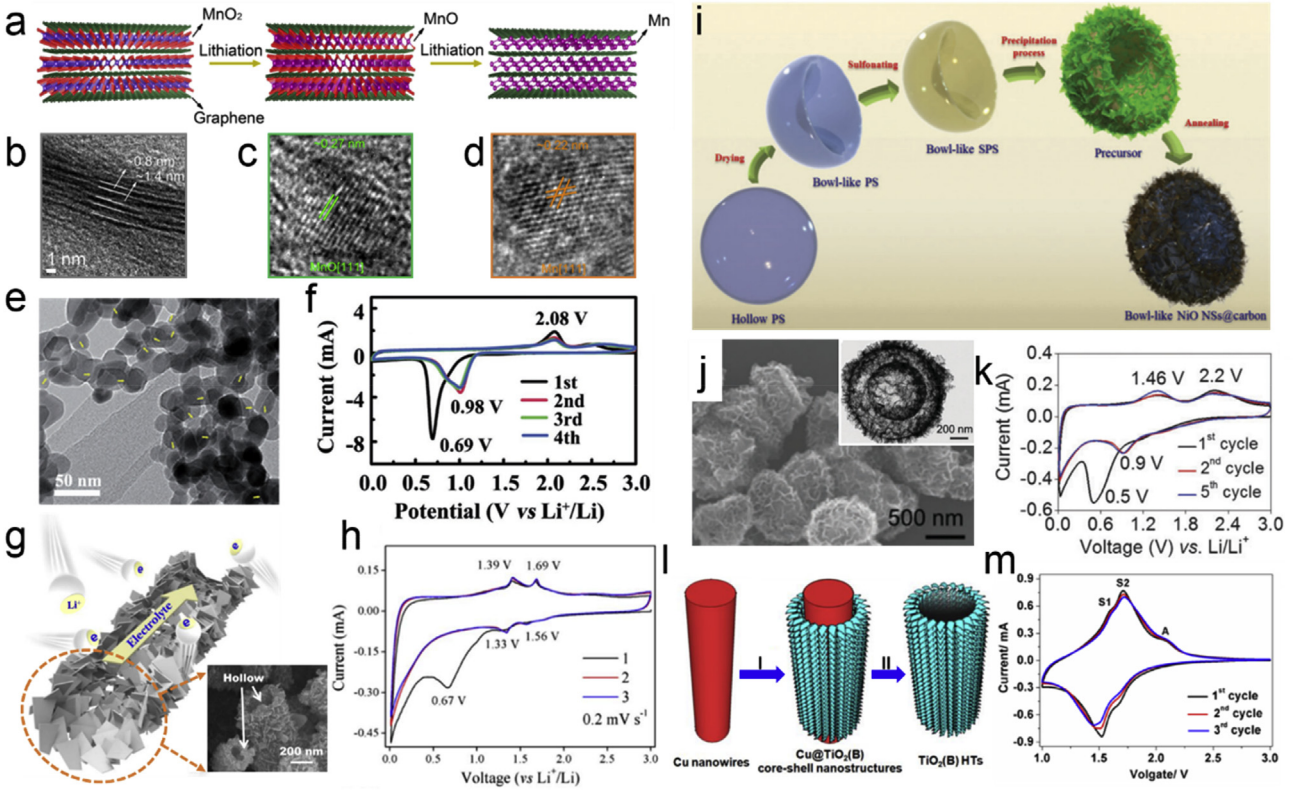

Fig. 2. (a) Two-step conversion process of the MnO_2/graphene superlattice during the first lithiation process. (b–d) HRTEM images of MnO_2, MnO and metallic Mn after lithiation. Reprinted with permission from Ref. [55]. Copyright 2018, ACS Publications. (e) TEM image of Co_3O_4 nanosheets. (f) CV curves of Co_3O_4 electrode. Reprinted with permission from Ref. [58]. Copyright 2017, Wiley Online Library. (g) The schematic illustration of the transport pathways of electrons, Li^+ and electrolyte in MoO_2 nanosheets. (h) CV curves of MoO_2 anode at a scan rate of 0.2 mV s^{-1}. Reprinted with permission from Ref. [65]. Copyright 2018, Elsevier. (i) Schematic illustration of the synthesis process of NiO NSs@C hybrid nanostructures. (j) The structural characteristics of NiO NSs@C. (k) Representative CVs at a scan rate of 0.5 mV s-1. Reprinted with permission from Ref. [69]. Copyright 2015, Royal Society of Chemistry. (l) Schematic illustration of the template-assisted formation of TiO_2 (B) hierarchical tubes. (m) CV curves of TiO_2 (B) between 1.0 and 3.0 V at a scan rate of 1 mV s^{-1}. Reprinted with permission from Ref. [74]. Copyright 2015, Royal Society of Chemistry.

On account of the improved safety and rate capability, titanium dioxide (TiO_2) has attracted extensive attention and frequently researched for LIB electrode material [72,73]. Hu and co-workers designed a kind of nanosheet-based tubular TiO_2 (B) structures via a facile solvothermal method using Cu nanowires as the template (Fig. 2l) [74]. CVs were conducted to further investigate the mechanism of Li storage (Fig. 2m). The distinct S peaks range from 1.5 V to 1.7 V assigned to pseudocapacitive behavior of Li^+ storage, while the less obvious A peaks at 1.7/2.0 V associated with the solid-state diffusion in the electrode, which indicates that lithiation-delithiation procedures are mainly owing to the surface-controlled pseudocapacitive process rather than the solid-state diffusion manner [75]. Due to the unique structural characteristics, these TiO_2 (B) hierarchical tubular structures provide high reversible Li^+ storage capacity (216 mA h g^{-1}) at 1C [74].

Except for the above-mentioned TMOs, tin dioxide (SnO_2) also has attracted intensive attention owing to the high theoretical specific capacity (781 mA h g^{-1}), on account of the reversible alloying/dealloying reactions between Sn and Li during the repeated charge/discharge processes. Unfortunately, the instinct poor electroconductivity of SnO_2 has hindered the practical applications. In order to address this problem, Min and coworkers designed a novel 3D hierarchical structure with amorphous carbon as the surface coating layer and carbon cloth as the backbone [76]. Such unique structure is promising for enhancing the conductivity due to the carbon cloth substrates, accommodating the volumetric changes due to the nanosheet structure, maintaining the structural integrity and avoiding the agglomeration of SnO_2 nanosheets owing to the coated carbon layer. Due to the above-mentioned advantages, this electrode can achieve a stable discharge capacity (656.2 mA h g^{-1}) at a high current density (1500 mA g^{-1}).

2.2. TMCs nanosheets

As a promising candidate to anode materials, graphene-like molybdenum disulfide (MoS_2, two-dimensional structure) has attracted extensive research interests due to its high theoretical capacity of 670 mA h g^{-1}, weak vdWs interaction and a comparatively larger interlayer distance of 0.62 nm, which can provide a facilitated transport path and rapid ion diffusion kinetics for Li^+ during the cycling charge/discharge process [77–79]. MoS_2 is a transition metal dichalcogenide composed of hexagonal layers. Each layer is referred to as a "monolayer" and consists of S–Mo–S laminate. A layer of Mo atoms is sandwiched between two layers of S atoms by a covalent bond.

Lu and co-workers designed a free-standing sandwich-like nanotube arrays composed of MoS_2 nanosheets through a facile template-based hydrothermal deposition process (Fig. 3a) [77]. Such unique structure possesses the following advantages. First of all, benefiting from the large amount of voids inside and outside the tube, the free-standing array nanostructure can greatly alleviate structural degrade during cycling, and preserve the nanotube array architecture even after repeated charge/discharge processes. In addition, the ion transport distance can be shortened as well as the reactive sites can be facilitated because of the ultra-thin walls of the hierarchical structure (Fig. 3b). Moreover, the movement of electrons from MoS_2 to outer conducting polymers (CPs) coating can be improved due to the synergistic coupling effect caused by the delocalized electrons between CPs conjugated π-bonds and Mo d orbitals [80,81]. Furthermore, the free-standing nanotube arrays can be

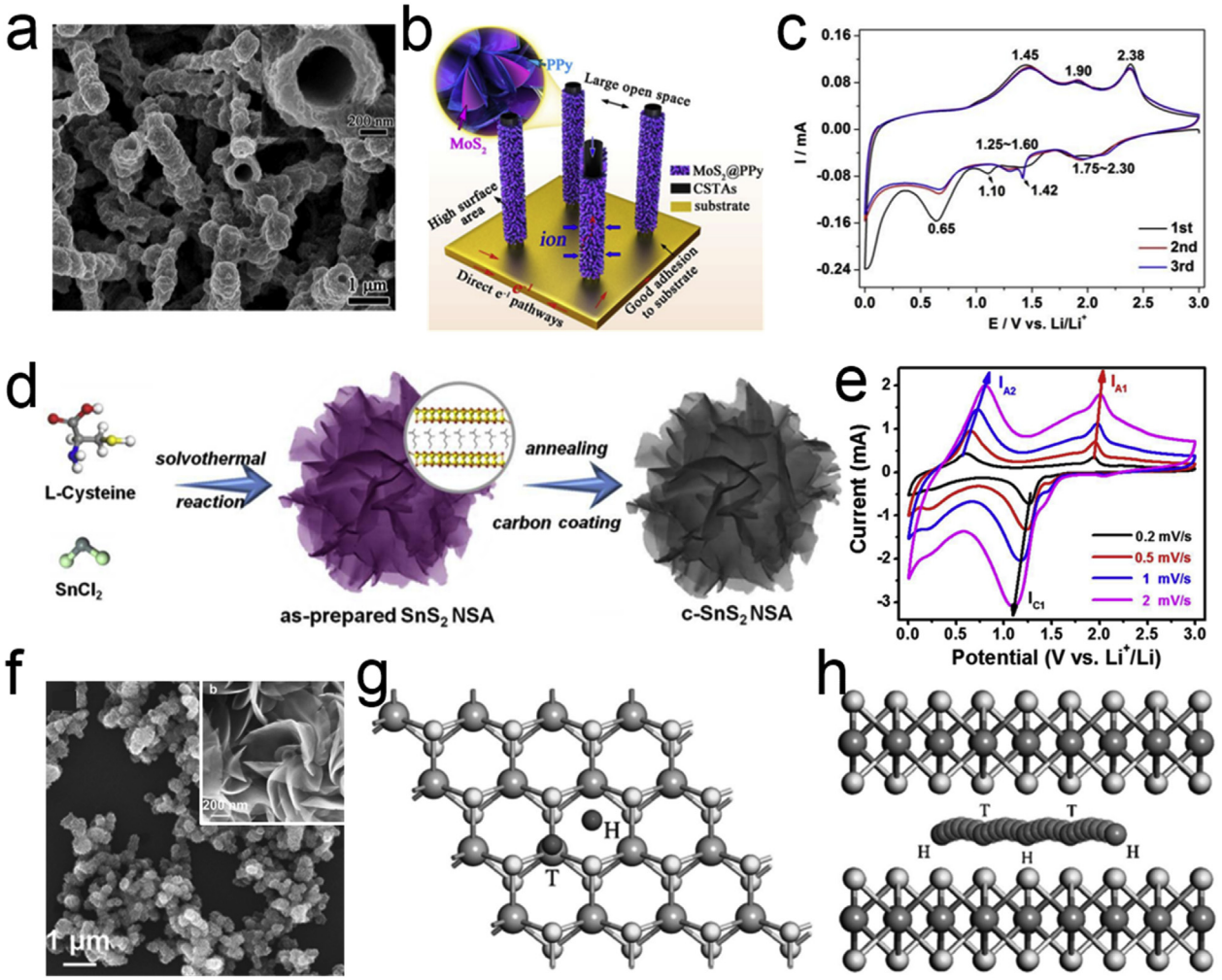

Fig. 3. (a, b) SEM image and schematic illustration of the free-standing sandwich-like MoS_2 nanotube arrays. (c) CV curves of MoS_2 nanotube arrays at 0.2 mV s^{-1}. Reprinted with permission from Ref. [77]. Copyright 2018, Elsevier. (d) Schematic illustration of the synthesis of SnS_2 nanosheet assemblies. (e) Stabilized CV curves of SnS_2 nanosheets at different scan rates. Reprinted with permission from Ref. [78]. Copyright 2017, Royal Society of Chemistry. (f) Morphology characterizations of VS_2 "nano-peony". (g) Two stable adsorption sites for Li^+ in the VS_2 bilayer. (h) Selected diffusion pathway of Li^+. Reprinted with permission from Ref. [93]. Copyright 2017, Wiley Online Library.

applied in the flexible devices due to the bendable electrode. The mechanism of Li^+ storage was investigated by CVs in a potential between 0.01 V and 3.0 V (Fig. 3c). Two broad waves over 1.75–2.30 V and 1.25–1.60 V can be observed clearly during the first discharge process, which correspond to the multistep insertion of Li^+ to form Li_xMoS_2 [82]. And the peaks around 1.10 V and 0.65 V are assigned to the formation of SEI, and the conversion from MoS_2 to metal Mo and Li_2S, respectively [83,84]. Three oxidation peaks at ca. 1.45, 1.90 and 2.38 V was detected in the anodic scan, which assigned to the progressive oxidation from Mo to Mo^{4+}, Mo^{4+} to Mo^{6+}, and the delithiation of Li_2S, respectively [85]. The overlapping cycling CV curves indicated the high electrochemical reversibility of the electrode. The reaction mechanism can be summarized as below:

$$MoS_2 + xLi^+ + xe^- \rightleftharpoons Li_xMoS_2 \quad (1)$$

$$Li_xMoS_2 + (4\text{-}x)Li^+ + (4\text{-}x)e^- \rightleftharpoons 2Li_2S + Mo \quad (2)$$

Hu and co-workers also designed a special 3D network structure via a reliable and facile preparation strategy, which can moderate the volume changes along with cycling procedures, facilite efficient transport and diffusion of Li^+, further afford continuous electro-conductive networks for e^- accelerated transfer [86]. Such 3D porous network architecture composed of hollow carbon spheres (HCS) cross-linked by rGO network, where the few-layered MoS_2 nanostructures were successfully grown onto the HCS and rGO.

In addition, because of the high theoretical capacity of 1230 mA h g^{-1}, SnS_2 has obtained extensive attention in energy storage field. SnS_2 possesses a CdI_2-type layered structure composed of a layer of tin atoms sandwiched between two layers of hexagonal closely packed sulfur atoms. Such a layered structure with a large layer spacing (0.5899 nm) should be easy to insert and extract from guest species and more easily accommodate volume changes in the host during cycling [87–89]. Wang and co-workers synthesized a kind of hierarchical SnS_2 nanosheet assemblies via a common solvothermal route as well as annealing and carbon coating procedures (Fig. 3d) [78]. CVs was performed under different scan rates to further investigate the mechanism of Li storage (Fig. 3e). Two peaks at 1.26 V and 1.50 V appear in the cathodic scan at 0.2 mV s^{-1}, which can be ascribed to the Li^+ intercalation into SnS_2 and the followed conversion process. In addition, the cathodic peak at ~0.7 V mainly on account of the electrochemical Sn/Li alloying processes [90]. Furthermore, other two anodic peaks (0.60 V and 1.95 V), respectively, was detected in the anodic scan, which attributed to the Sn/Li dealloying and followed back reaction to SnS_2 [91]. As can be seen, the current values of peaks become larger, simultaneously, the positions of the current vertexes were shifted with the increasing of rate [78]. Due to the large specific surface area and rich

active sites caused by nanosheet morphology, SnS_2 nanosheet assemblies exhibit an enhanced high specific capacity (~1200 mA h g^{-1} at 0.2 A g^{-1}) compared with SnS_2 nanopowders (~400 mA h g^{-1}).

Among the transition metal oxides (TMCs), VS_2 monolayer was metallic, unlike MoS_2, which is semiconducting, thus possesses a faster Li^+ diffusion rate than MoS_2 [92]. Zhou and co-workers prepared hierarchical VS_2 "nano-peony" composed of aligned ultrathin nanosheets via a simple solvothermal process [93]. The obtained VS_2 "nano-peony" was composed of many curved nanosheets that were oriented to different angles (Fig. 3f). As illustrated in Fig. 3g, Density functional theory (DFT) calculations suggested that there are two stable sites between VS_2 layers, the hexagonal (H) site and tetrahedral (T) site, which is above the center of the hexagonal ring and on the top of V atom, respectively. Li^+ preferred the T site of VS_2 layers because of the higher adsorption energy than that of the H site, and thus form a stable intercalation compounds [94]. In addition, the simulation of ionic diffusion between VS_2 layers shows that the diffusion barrier is sufficiently low, which means the fast ionic diffusion within layered VS_2 (Fig. 3h). The hierarchical arrangement of VS_2 nanosheets can effectively impede the restack, thus can boost the exposed surface areas, provide mass transport path, and alleviate volume change accompanying with the charge/discharge processes. Thus, VS_2 nanosheets enabled rapid and stable storage of lithium with a high specific capacity (1050 mA h g^{-1}) at 0.1 A g^{-1} [93].

Niobium disulfide (NbS_2) with high theoretical specific capacity of 683 mA h g^{-1} and good electroconductivity is another promising candidate for lithium ion batteries [95] as well as benefiting from the low band gap and conversion processes during the cycles ($NbS_2 + 4Li^+ + 4e^- \leftrightarrow Nb + 2Li_2S$, Fig. 4a). Zhang and co-workers synthesized uniform doped NbS_2 nanosheets through a simple oil-phase preparation method [96]. As can be seen from Fig. 4b, the b value of 0.83 for Fe and Se co-doped nanosheets ($Fe_{0.3}Nb_{0.7}S_{1.6}Se_{0.4}$) indicates an apparent capacitive Li^+ storage. Furthermore, the capacitive contribution is around 81.2% at 1 mV s^{-1} (Fig. 4c), which benefits from abundant reaction sites after doped as well as high surface area [96].

Merits in the comparative interlayer spacing (6.14 Å) with MoS_2, extremely weak mutual attraction of interlayers, Rhenium disulfide (ReS_2, theoretical specific capacity: 430 mA h g^{-1}), new member of TMCs family, is regarded as another potential anode for energy storage [97–99]. Mao and co-workers proposed novel ReS_2 nanosheets uniformly anchored on N-doped carbon nanofibers (Fig. 4d) via a facile electrospinning and following by hydrothermal treatment [100]. Such nanostructure possesses the following advantages, fast electronic/ionic transportation path, outstanding electrochemical stability property during repeated charge/discharge process, and extremely weakly van der Waals interaction of ReS_2 layers. To further investigate the mechanism of Li^+ storage processes, CV curves of ReS_2/N-CNFs were tested at the range of 0.01 and 3 V (Fig. 4e). Two obvious reduction peaks at ca. 1.32 and 0.71 V appears in the 1st discharge process (rate: 0.1 mV s^{-1}), which attributed to the Li^+ insertion to ReS_2 layers (equation (3)), and the conversion from Li_xReS_2 to Li_2S and metallic Re (equation (4)), together with the formation of SEI. In the charge process, other two peaks at 1.83 V and 2.33 V were detected, due to the formation of Li_xReS_2 as well as ReS_2, respectively [101].

$$ReS_2 + xLi^+ + xe^- \rightarrow Li_xReS_2 \quad (3)$$

$$Li_xReS_2 + (4\text{-}x)Li^+ + (4\text{-}x)e^- \rightarrow Re + 2Li_2S \quad (4)$$

As can be seen, the CV peak positions were slightly shifted during the following two scans. The two discharge peaks shifted from ca. 1.32 V and 0.71 V to ca. 2 V and 1.23 V, which owing to the relaxation of stress, meanwhile, the anodic peak at 1.83 V shifted to higher voltage and almost merged with the anodic peak at 2.33 V [100].

VSe_2, as a layered metallic TMC, has attracted extensive attention in energy related field because of the metallic properties result from strong electron coupling interaction between V^{4+}-V^{4+} pairs, and the similar layered structure like MoS_2 [102,103]. Ming and co-workers reported a simple one-pot approach to acquire the ultrathin VSe_2 nanosheets with ca. 5 nm thickness carbon coating layer (Fig. 4f and g), which can buffer the volumetric change of VSe_2 electrode during repeated lithiation/delithiation process and maintain the ion transport path [104]. CVs was performed to further study the Li^+ storage processes (Fig. 4h). A broad discharge peak centered at 0.41 V in the 1st cycle corresponds to the SEI formation. Similar to the above-mentioned VS_2, the peak pairs of 2.0/2.23 V and 1.43/1.83 V are detected, which attributed to the intercalation reaction and conversion reaction, respectively [104].

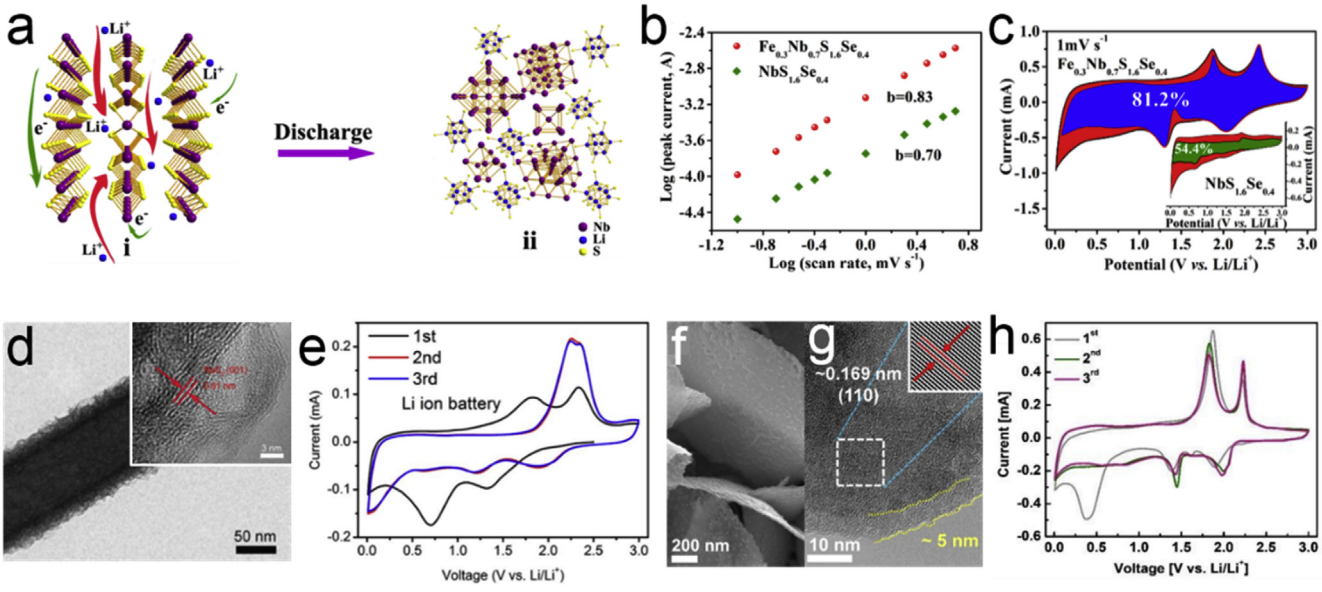

Fig. 4. (a) Schematic illustration of the conversion reaction mechanism for NbS_2. (b) Values of b of $Fe_{0.3}Nb_{0.7}S_{1.6}Se_{0.4}$ nanosheets. (c) Capacitive contribution of $Fe_{0.3}Nb_{0.7}S_{1.6}Se_{0.4}$ nanosheets at 1 mV s^{-1}. Reprinted with permission from Ref. [96]. Copyright 2017, ACS Publications. (d) TEM image of ReS_2 nanocomposites. (e) CV curves of ReS_2 nanocomposites at a scan rate of 0.1 mV s^{-1}. Reprinted with permission from Ref. [100]. Copyright 2018, Elsevier. (f, g) SEM image and HRTEM image of VSe_2 nanosheets. (h) CV curves of VSe_2 nanosheets. Reprinted with permission from Ref. [104]. Copyright 2018, Elsevier.

2.3. Other type nanosheets

In recent years, another constantly explored 2D layered MXene material, Ti_3C_2, were considered as the potential anode in energy storage field, owing to the advantages of tunable interlayer distance, high conductivity, as well as adjustable surface property [105,106]. DFT computations revealed fast Li^+ diffusion and high rate performances of Ti_3C_2 based anodes, which is attributed to the low Li diffusion barrier of Ti_3C_2 [107,108]. Meng and co-workers introduced black phosphorus quantum dots (BPQDs) into well-dispersed Ti_3C_2 nanosheets (TNS) via a liquid-solid-phase assembly strategy, coupled with sonication and freeze-drying processes (Fig. 5a), where BP boosts charge carrier mobility and Ti_3C_2 provides efficient electron transport pathway as well as enhances Li storage capacity [109]. The surface of Ti_3C_2 nanosheets are completely decorated by BPQDs (Fig. 5b), and two distinct lattice spacings (0.153 nm, 0.342 nm) respectively corresponds to the (110) plane of Ti_3C_2, and (040) plane of BP (Fig. 5c). In addition, a kind of mechanism named dual-model energy storage (DMES) was proposed to demonstrate the excellent electrochemical performances. As can be seen from Fig. 5d, extra pseudocapacitive storage reactions are occurred once the discharge process start (Step I). Li^+ from electrolyte solution stored in the C and O sites, meanwhile, electrons transported to corresponding Ti ions. While, only electrons transported to positive P elements through P–O–Ti bonds. Afterwards, alloying (BPQD) and pseudocapacitive (TNS) processes are generated (Step II). Accordingly, the DMES mechanism can be summarized as follows. First of all, BPQDs provide sufficient sites for Li^+ storage, as well as decrease the Li^+ transport distances, which indicates an alloying manner. In addition, TNSs afford active surface groups and high surface area, which are beneficial for pseudocapacitive Li^+ storage, thus achieve high rate performances. Furthermore, the combination of BPQDs and TNSs is of vital importance to achieve the extraordinary electrochemical performances [109]. Except for being used as an active material, the MXene nanosheets can also be employed as the stable substrates to support TMO materials thus preventing them from aggregation, as well as enhancing ion transportation efficiency at the interfaces. Liu and co-workers found that when TMOs and MXene nanosheets are mixed in THF solution, TMOs will be assembled on the surface of MXene nanosheets by vdWs interactions, thereby minimizing the surface energy of MXene and forming micellar heterostructures to stabilize the whole system [110]. Based on this discovery, they designed TiO_2/MXene and SnO_2/MXene heterostructures, and achieved outstanding rate performances (TiO_2/MXene: 272, 250, 233, 204 mA h g^{-1} at 50, 100, 200, 500 mA g^{-1}; SnO_2/MXene: 720, 665, 606, 560 mA h g^{-1} at 100, 200, 500, 1000 mA g^{-1}).

Highly doped porous graphene via supramolecular polymerization and annealing process were successfully developed by our group (Fig. 4e) [111]. The melamine cyanurate supramolecular polymer holds the following three missions, to avoid graphene restacking as a barrier, to acquire the porous structure by template sacrifice, to obtain the nitrogen atoms for further doping process. Thus, N doped graphene with porous and loose-packed layer structure was obtained after the annealing procedure (Fig. 5f). CVs was conducted to further investigate the mechanism of Li storage (Fig. 5g), which reflected the typical shape of Li^+-carbon reaction. A pronounced discharge peak (0.3–0.9 V) appears during the 1st cycle, which can be ascribed to the SEI formation [112,113]. In the subsequent cycles, the CV curves are almost overlapped, which indicates that a stable SEI layer is formed during the previous discharge process. Furthermore, our group also fabricates a kind of N/S co-doped graphene for better carbon-based LIB anodes [114]. In this approach, 2-aminothiophenol (ATP) was utilized as both N source and S source. The obtained NS-G is regarded as a superb anode because of the outstanding electrochemical properties, benefiting from the synergistic effects and unique structural features.

Current strategies for preparing 2D materials are usually classified into two routes [115]. Liquid-phase methods, involving liquid-exfoliation [116] and chemical synthesis [117], are usually simple, scalable, and capable of generating uniform samples, but a serious of complicated purification procedures are needed for post-treatment procedure [118]. Gas-phase methods, such as chemical vapor deposition (CVD), typically produce big and broad 2D nanosheets with good quality [119]. However, the large scale applications are seriously limited by low output and high cost [120]. As a result, developing a universal strategy, which can simultaneously possess the both advantages of liquid-phase and gas-phase syntheses, is extremely desirable. Wang and co-workers proposed a novel “gel-blowing” strategy, which can rapidly (within 1 min) and thermally expand the viscous gel and thus acquire large

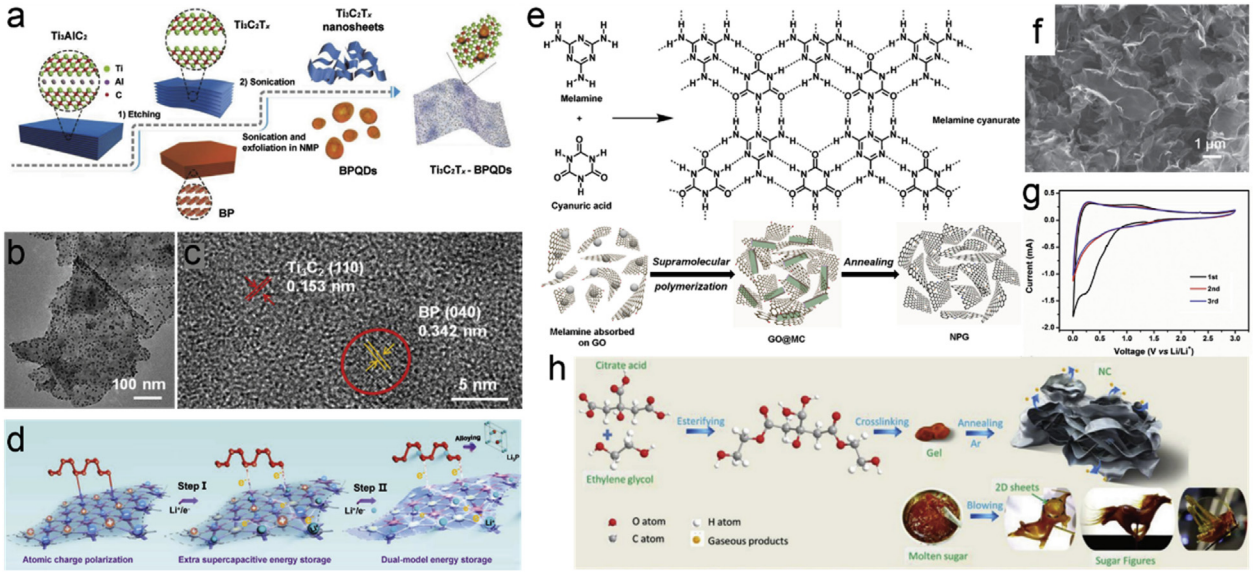

Fig. 5. (a) Schematic illustration of the formation process of the Ti_3C_2 nanocomposite. (b, c) TEM image and HRTEM image of Ti_3C_2 nanocomposite. (d) Schematic illustration of the DMES mechanism of Ti_3C_2 nanocomposite electrode. Reprinted with permission from Ref. [109]. Copyright 2018, Wiley Online Library. (e) Schematic illustration of the synthesis procedure of N doped graphene. (f) SEM image of N doped graphene. (g) CV curves of the N doped graphene electrode at a scanning rate of 0.5 mV s^{-1}. Reprinted with permission from Ref. [111]. Copyright 2015, Wiley Online Library. (h) Proposed formation machenism of 2D NC nanosheets. Reprinted with permission from Ref. [121]. Copyright 2018, Wiley Online Library.

Table 2
Summary of synthesis methods and electrochemical properties of various kinds of nanosheets for SIBs.

Materials	Synthesis method	Electrochemical performance				Ref.
		Coulombic efficiency	Initial capacity	Rate capability	Cycling stability	
Co_3O_4	precipitation and post-annealing	55% (1st)	553 mA h g^{-1} (0.1 A g^{-1})	175 mA h g^{-1} (1.6 A g^{-1})	300 mA h g^{-1} (100th cycle at 0.8 A g^{-1})	[60]
K_xMnO_2	precipitation	–	75 mA h g^{-1} (0.08 A g^{-1})	50 mA h g^{-1} (0.2 A g^{-1})	52 mA h g^{-1} (500th cycle at 0.08 A g^{-1})	[129]
TiO_2	hydrothermal and post-annealing	40% (1st)	226 mA h g^{-1} (0.2 mA g^{-1})	116 mA h g^{-1} (10 A g^{-1})	120 mA h g^{-1} (3600th cycle at 2 A g^{-1})	[130]
MoS_2	hydrothermal and post-annealing	–	416 mA h g^{-1} (0.1 A g^{-1})	141 mA h g^{-1} (12.8 A g^{-1})	198 mA h g^{-1} (1000th cycle at 1 A g^{-1})	[137]
WS_2	solvothermal method	–	401 mA h g^{-1} (0.1 A g^{-1})	151 mA h g^{-1} (5 A g^{-1})	78 mA h g^{-1} (500th cycle at 5 A g^{-1})	[142]
V_5S_8	chemical exfoliation	–	701 mA h g^{-1} (0.1 A g^{-1})	190 mA h g^{-1} (10 A g^{-1})	385 mA h g^{-1} (100th cycle at 1 A g^{-1})	[144]
SnS_2	hydrothermal and post-annealing	74% (1st)	823 mA h g^{-1} (0.1 A g^{-1})	378 mA h g^{-1} (12.8 A g^{-1})	701 mA h g^{-1} (200th cycle at 0.2 A g^{-1})	[148]
SnS	hot bath route	81% (1st)	1416 mA h g^{-1} (0.03 A g^{-1})	400 mAh g^{-1} (30 A g^{-1})	1010 mA h g^{-1} (200th cycle at 0.1 A g^{-1})	[149]
Graphene	hydrothermal method	–	183 mA h g^{-1} (0.1 A g^{-1})	61 mAh g^{-1} (8 A g^{-1})	105 mA h g^{-1} (500th cycle at 1 A g^{-1})	[155]
SnP_2S_6	hydrothermal and post-annealing	60.8% (1st)	1253 mA h g^{-1} (0.05 A g^{-1})	118 mAh g^{-1} (20 A g^{-1})	500 mA h g^{-1} (1000th cycle at 2 A g^{-1})	[157]

amount of nanosheets [121]. This novel approach integrate both advantages of the above-mentioned two strategies, which can generate nanosheets with nanoscale thickness, big lateral sizes, good homogenization, as well as mass production in short time. The proposed formation principle of 2D N-doped carbon (NC) nanosheets is demonstrated in Fig. 5h. Firstly, ethylene glycol and citric acid react to form the cross-linked polyester in the sol-gel process. Afterwards, in the rapid thermal process, the dehydration and redox reactions would generate and release gases (such as H_2O, CO_2, and N_2), which can effectively blow the polyester gel, and as a result, the walls become ultrathin. Furthermore, under a high temperature, the polymeric walls convert into solid carbon then ultrathin nanosheets after bubbles crushed and/or collapsed. This process is quite similar with the process of Sugar Figure Blowing Art, which typically composed of expanding, solidifying, and shaping procedures [121].

As mentioned above, since graphene possesses such many benefits as enhanced conductivity, shortened diffusion pathways, and inhibited volume changes, is it better to combine graphene with other kinds of high-capacity materials for ion storage? Mei and co-workers designed a novel 2D-TiO_2-2D vdWs heterostructured anode with BP nanosheets and porous graphene layer linked by TiO_2 nanoparticles. Except for the above-mentioned advantages of graphene, the restack between nanosheets can be effectively prevented, and the interfacial ion storage can be obviously enhanced as well. The 2D-TiO_2-2D anode is able to achieve a high discharge capacity (1336.1 mA h g^{-1}) at a current density of (200 mA g^{-1}) [122].

Enhancing the mass loading of electrochemically active materials is of great significant to realize high areal capacity of batteries. Unfortunately, the large volume change caused by electrode materials with alloying/dealloying and conversion mechanisms, such as SnO_2, Fe_3O_4, and Co_3O_4, is detrimental to the stability of the high mass loading electrodes. Xu and co-workers synthesized a new vanadium-based anode, nanosheet-assembled compact CaV_4O_9 "micro-peony", via a simple hydrothermal route, which can not only alleviate the mechanical stress accompanying with the electrochemical reaction, but also render the multi-electron transfer due to the multivalent property of vanadium as well, and thus achieve high specific capacity [123]. Merits in the enhanced space utilization and tap density, shortened ion diffusion distance, as well as exposed active sites, the as-designed electrodes acquire excellent Li^+ storage performance (specific capacity: ~2.5 mA h cm^{-2}; cycle numbers: 400; final capacity: 1.5 mA h cm^{-2}). The thickness of CaV_4O_9 based electrode shows a small change after prolonged electrochemical cycles, indicating the excellent structure stability of nanosheet assemblies.

In addition to the above materials, silicon (Si) has attract great interest due to the high theoretical capacity of 4200 mA h g^{-1} and low discharge potential (~0.1 V vs. Li/Li^+). Unfortunately, poor electrical conductivity, the large volume change, and serious degradation of unstable SEI layer have greatly hindered the practical applications of Si based electrodes [124,125]. Ultrathin Si nanosheets with a high yield of ~40% were synthesized through a two-step process (pre-exfoliated silicate sheets and subsequent chemical reduction) [126]. This kind of Si nanomaterials holds the unique advantages of easy accessibility of lithium ions, as well as small volume expansion during the repeated lithiation/delithiation process. Therefore, high specific capacity (865 mA h g^{-1} at 0.5C), excellent cycling stability (500 cycles at 0.5C) with suppressed volume expansion (42% after 200 cycles) can be obtained in Li^+ storage system.

A new synthesis strategy to prepare large-scale and high-quality silicene nanosheets via liquid oxidation and exfoliation of $CaSi_2$ is developed by Liu and co-workers [127]. Firstly, by using I_2 as the oxidant, oxidizing $CaSi_2$ under room temperature to obtain insufficiently exfoliated $CaSi_2$ with the intermediately loose stacking structure. After that, fully exfoliated silicene nanosheets with monolayer or few-layer structures were obtained via utilizing ultrasonic exfoliation and centrifugation methods. The obtained silicene nanosheets possess high crystallinity and display a high capacity (721 mA h g^{-1} at 0.1 A g^{-1}), which almost reaches the theoretical capacity of double-layer silicone.

3. Nanosheet-based materials for SIBs

Due to the abundance of sodium resources all over the world as well as the cost considerations, SIBs attracted numerous studies very recently. Because of the relative ionic radius (Na^+: 1.02 Å; Li^+: 0.76 Å), designing and manufacturing more advantageous material structures for Na^+ storage is a rigorous challenge. Table 2 summarized the common employed materials for Na^+ storage (Co_3O_4, K_xMnO_2, TiO_2, MoS_2, SnS_2, WS_2, V_5S_8, SnS_2, graphene, and SnP_2S_6, etc.). As can be seen, these materials display excellent rate capability. However, the Coulombic efficiency of the first cycle is relatively low (40–80%), thus developing effective methods to solve this defect are urgently expected.

3.1. TMOs nanosheets

Co_3O_4 nanosheets with controllable pore size and pore architecture was prepared by Chen and co-workers for SIB anodes [60]. In-situ TEM characterization is employed to describe and further understand the structural evolution during the sodiation process. Due to the well dispersed Co in a Na_2O matrix, the 2D Co_3O_4 nanosheets can maintain the porous morphology during the sodiation process. As a result, the obtained 2D Co_3O_4 shows a relatively small volume expansion than the

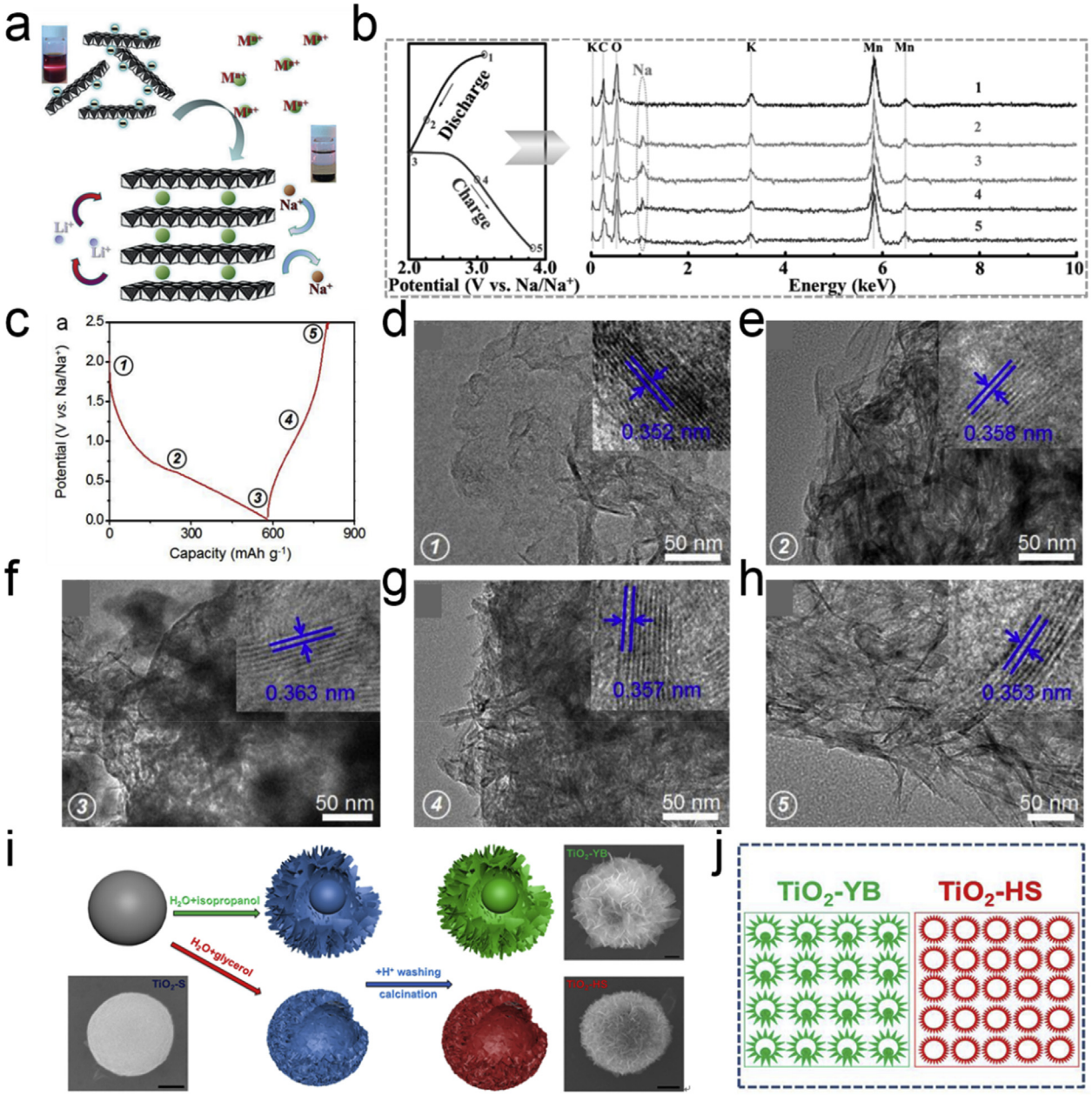

Fig. 6. (a) Preparation of 3D layered manganese oxide frameworks. (b) Discharge/charge curves and corresponding EDX spectra of K_xMO_2 at different discharge/charge stages in the first cycle. Reprinted with permission from Ref. [129]. Copyright 2016, Wiley Online Library. (c) The initial galvanostatic charge/discharge profiles of OVs-TiO_{2-x}. (d–h) Ex-situ TEM images of wrinkled OVs-TiO_{2-x} at different charge/discharge stages: (d) stage 1, (e) stage 2, (f) stage 3, (g) stage 4, and (h) stage 5. Reprinted with permission from Ref. [130]. Copyright 2018, Elsevier. (i, j) Preparation routes of different TiO_2 spheres and the reason of improving packing density. Reprinted with permission from Ref. [133]. Copyright 2019, Wiley Online Library.

traditional Co_3O_4 particles. This 2D porous nano-architecture can hinder the restacking of nanosheets and accommodate the volume expansion as well for superior Na ion storage.

For another kind of TMO, manganese dioxides have been extensively studied because of the attractive theoretical capacity, structural diversity, and natural abundance [128]. Lu and co-workers proposed a bottom-up strategy for fabricating hierarchical frameworks, which are composed of K_xMnO_2 (Fig. 6a) [129]. Energy-dispersive X-ray (EDX) spectra of K_xMnO_2 along with the cycle process were performed to study the related mechanisms of Na^+ storage (Fig. 6b). During the discharging process from point 1 to point 3, the concentration of Na^+ shows a gradual increase until reach the maximum value, which corresponding to the intercalation of Na^+. Afterwards, the Na^+ was deintercalated from K_xMnO_2 during the charging process from point 3 to point 5. After one intercalation/deintercalation cycle, the concentration of Na^+ restored to the initial state, indicating the good reversibility of K_xMnO_2 anode [129].

Ma and co-workers introduced electroconductive titanium oxide (TiO_{2-x}) nanosheets with rich oxygen vacancies (OVs) and electroconducting Ti^{3+} species as the anode of SIBs [130]. Merits in the reduced the Na^+ diffusion length, enhanced conductive networks, and boosted electron transfer, the obtained products possess fast kinetics of Na^+ diffusion and adsorption [131], and thus display excellent Na^+ storage property with the reversible capacity of 230 mA h g^{-1} at 100 mA g^{-1}, as well as long-term cycling performance at high current rate. Further improvement of electrochemical performances can be achieved via combining with graphene sheets. Benefiting from synergistic effect of graphene preservation networks and rich OVs defects, the electrode exhibits a relatively higher capacity of 153 mA h g^{-1} at a high

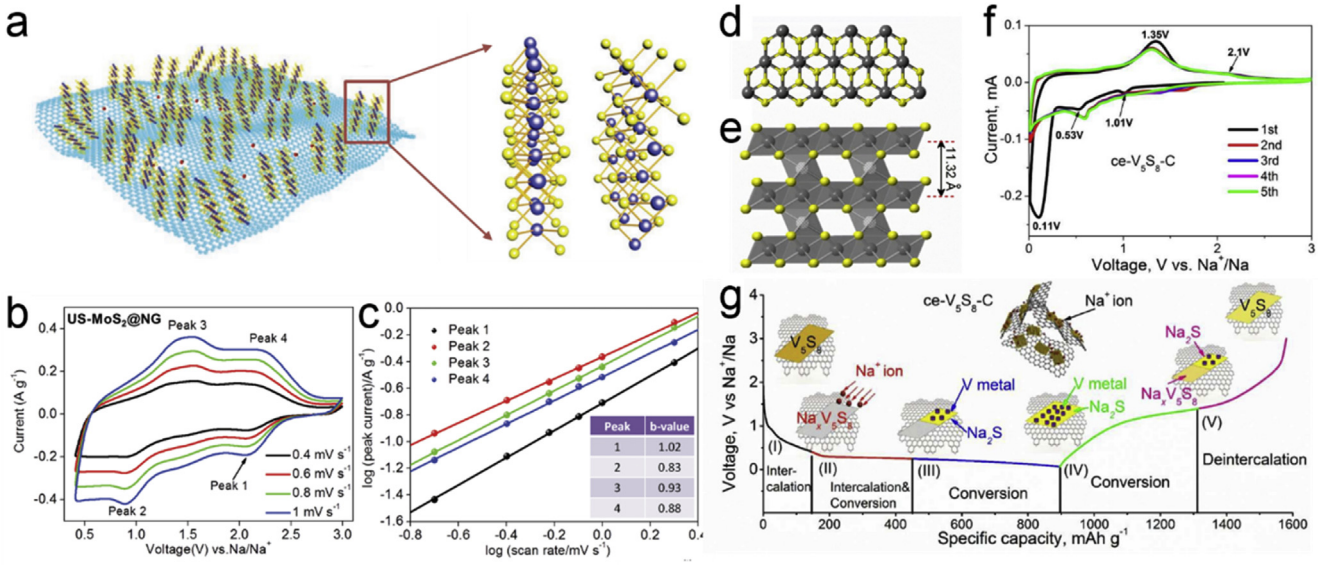

Fig. 7. (a) Schematic illustration of the morphology and crystal structure of MoS_2 nanosheets@NG. (b) CV curves at different scan rate. (c) Logarithm peak current versus logarithm scan rate plots. Reprinted with permission from Ref. [137]. Copyright 2018, Wiley Online Library. (d) The top-view and (e) side-view of atoms arrangements in V_5S_8. (f) CV of V_5S_8 anode at the scan rate of 0.1 mV s^{-1}. (g) Schematic illustration of the energy storage mechanism of the V_5S_8 anode. Reprinted with permission from Ref. [144]. Copyright 2017, Royal Society of Chemistry.

current density of 6700 mA g^{-1} [132]. To further study the Na^+ storage mechanisms, ex-situ HRTEM and TEM characterizations were employed during Na^+ reaction cycles (Fig. 6c–h). As can be seen, the lattice spacings varies from 0.352 nm to 0.363 nm from stage 1–3, which corresponding to the insertion of Na^+ into OVs-TiO_{2-x} structures. Afterwards, the observed lattice spacings recovered to 0.353 nm at stage 5, which attributed to the extraction of Na^+ (Fig. 6g and h). The varying lattice spacings at different charge/discharge stages indicate the stability of the as-prepared samples accompanying with the Na^+ insertion and extraction processes. Based on this, the possible Na^+ storage mechanisms can be summarized as followed points. On one hand, the Introducing of abundant OVs is able to greatly improve the electrical conductivity of electrodes. On the other hand, the introduced OVs also significantly lead to the lattice spacing expansion, which ensure the fast kinetics of Na^+ insertion/extraction [130]. In addition, our group rationally controlled the morphology and structure of TiO_2 spheres to optimize their Na^+ storage performances (Fig. 6i). The as-prepared yolk-like spheres with bigger nanosheets (TiO_2-HS) possess higher packing density than that of hollow spheres formed by smaller nanosheets (TiO_2-YB) due to the reasonable design of extrinsic nanosheets, which is beneficial to increasing the volume energy density of batteries (Fig. 6j). Moreover, the Na^+ storage kinetics of the TiO_2 spheres are affected by the varieties of interiors and shells, resulting in stepwisely improved pseudocapacitance responses and rate performances [133].

Molybdenum trioxide (MoO_3) is another insertion and conversion reaction based electrode materials. Owing to the high theoretical capacity (1117 mA h g^{-1}) and thermodynamical stablility, orthorhombic α-MoO_3 is regarded as a candidate for Na storage. Wu and co-workers synthesized novel flexible α-MoO_3 nanosheets on the surface of carbon fiber cloth via a facial solvothermal method and then followed by a thermal oxidization process [134]. The obtained 3D hierarchical architectures illustrate outstanding Na^+ storage behavior (capacity: 2.5 mA h cm^{-2} at 0.1 mA cm^{-2}), which is much higher than that of MoO_3 powder (capacity: 2.0 mA h cm^{-2} at 0.1 mA cm^{-2}), and long-term cycling stability over 200 charge-discharge cycles at higher rate. The excellent electrochemical performance of 3D hierarchical architectures can be assigned to the following factors. Firstly, the high surface areas are able to afford many Na^+ storage active positions. In addition, the free-standing electrodes can effectively reduce the side reactions. Furthermore, with respect to the good rate and cycling performances, the capacitive factor also participate in the performance further improvement [134].

3.2. TMCs nanosheets

MoS_2, a kind of TMCs with large layer distance and promising host material, was extensively investigated in Na^+ storage field [135]. The mechanism of Na^+ storage is generally agreed in the following two equations [136,137].

$$MoS_2 + x\ Na = Na_xMoS_2\ (\text{above } 0.4\ V,\ x < 2) \quad (5)$$

$$Na_xMoS_2 + (4\text{-}x)\ Na = Mo + 2Na_2S\ (\text{below } 0.4\ V) \quad (6)$$

Ultrasmall (US) MoS_2 nanosheets coupled with previously introduced nitrogen doped graphene (NG) samples were designed by our group via a simple solvothermal approach [137]. The obtained vertical US-MoS_2 nanosheets possess lateral sizes of 10–50 nm (Fig. 7a). The as-prepared US nanosheets are able to significantly decrease the Na^+ diffusion distances and energy barriers. Moreover, the decreased nanosheet size can provide more active sites for Na^+ insertion/extraction. Furthermore, the NG constituent can also enhance structural stability and electroconductivity of the whole electrode. Benefiting from those above-mentioned advantages, the US-MoS_2 nanosheets@NG composite shows superior sodium intercalation performance under voltage window of 0.4–3 V. Fig. 7b shows that similar shapes of CV curves with two redox couples can be detected, which indicates an obvious pseudocapacitive behavior. As can be seen from Fig. 7c, the b values of different peaks are obtained as 1.02, 0.83, 0.93, and 0.88, respectively, which indicate that Na^+ storage process is mainly complied with the surface-controlled kinetics [137,138].

A novel low-cost, high-yield, and scalable synthesis approach with ball-milling and physical exfoliation process was developed by Sun and co-workers for preparing MoS_2/graphene hybrids [139]. The as-prepared MoS_2/graphene hybrid anode material exhibits outstanding electrochemical performances (cycling and rate results), which can be ascribed to the improved conductivity and decreased Na^+ diffusion barrier at the interfaces of MoS_2/graphene hybrids caused by the low degree of defects and oxygen containing groups in graphene. In order to improve the

mechanical stability, conductivity, and active material utilization of MoS_2, which are three key challenges related to MoS_2 electrodes. Wang and co-workers controllably synthesized MoS_2 nanosheets vertically anchored on the exfoliated graphene (EG) by a solution strategy [140]. The as-obtained hierarchical structure can overcome the above problems simultaneously owing to the interconnected network, inseparable contact between EG and MoS_2 nanosheets, as well as the exposed active sites. As a result, EG-MoS_2 with 95 wt% MoS_2 content can deliver an ultrahigh specific capacities of 509 mA h g^{-1} at 1 A g^{-1} for Na^+ storage.

Among other TMCs, 2D tungsten disulfide (WS_2) has also attracted extensive attention [141]. Lim and co-workers reported a simple solvothermal route to prepare nitrogen doped carbon nanocubic framework with an outer shell of vertical WS_2 nanosheets [142]. Such nano-architectures (WS_2@NC) possess the next introduced superiorities. On one hand, the carbon framework boosts conductivity of the electrode, mitigates the volume expansion during the repeated sodiation/desodiation cycles, as well as reduces the diffusion distance of the Na^+, which guarantees the rapid ionic transport. On the other hand, integration with 2D nanosheets, the unique nano-architectures (2D-3D hybrid) afford more active surface area for Na^+ insertion/extraction [143]. CV measurements indicated two-step reaction mechanisms of Na^+ storage as follows, which are similar with MoS_2:

$$4\ Na^+ + WS_2 + 4e^- \rightarrow Na_4WS_2 \quad (7)$$

$$Na_4WS_2 \rightarrow W + 2Na_2S \quad (8)$$

Yang and co-workers prepared a new 3D compound monoclinic structured V_5S_8 with unique crystal structure (Fig. 7d and e) [144]. Accordingly, the generation and transportation of different charge carriers were enhanced by such unique structure, thus increase electronic/ionic conductivity, and promote the fast diffusion transport of electrons and Na^+ during the sodiation/desodiation process. The CVs were also tested aim to study the Na^+ storage mechanisms (Fig. 7f). In the first scan, the characteristic peaks at 1.01, 0.53 and 0.11 V, respectively, can be attributed to the Na^+ insertion into V_5S_8 together with the formation of SEI, partial sodiation to form $Na_xV_5S_8$, and further sodiation to form Na_2S and V, respectively. While, the two obvious charge peaks at 1.35 and 2.1 V, are related to the conversion reaction between Na_2S and V, and desodiation to generate V_5S_8, respectively [144]. The Na^+ storage mechanism of V5S8 anode was further revealed by in situ XRD (Fig. 7g), the corresponding desodiation/sodiation processes can be summarized by the following equations:

$$Na^+ \text{ intercalation: } V_5S_8 + x\ Na^+ + x\ e^- \rightarrow Na_xV_5S_8\ (>0.4\ V) \quad (9)$$

$$\text{and partial } Na^+ \text{ conversion: } Na_xV_5S_8 + (16\text{-}x)\ Na^+ + (16\text{-}x)\ e^- \rightarrow 8\ Na_2S + 5\ V\ (0.4\text{–}0.25\ V) \quad (10)$$

$$\text{Full } Na^+ \text{ conversion: } Na_xV_5S_8 + (16\text{-}x)\ Na^+ + (16\text{-}x)\ e^- \rightarrow 8\ Na_2S + 5\ V\ (<0.25\ V) \quad (11)$$

The reverse reaction (12) and (13) take place at <1.35 V and >1.35 V, respectively, during the charging process.

$$8\ Na_2S + 5\ V \rightarrow Na_xV_5S_8 + (16\text{-}x)\ Na^+ + (16\text{-}x)\ e^-\ (\text{˚}1.35\ V) \quad (12)$$

$$Na_xV_5S_8 \rightarrow V_5S_8 + x\ Na^+ + x\ e^-\ (\text{˚}1.35\ V) \quad (13)$$

Different from most TMCs with semiconductivity, VS_2 nanomaterials is metallic, thus possess the excellent conductivity, and shows greatly improved electrochemical performance. Wang and co-workers synthesized VS_2 nanosheets via a simple hydrothermal method [145]. Ex situ TEM examination was carried to further explore the phase transformations of VS_2 during Na^+ insertion/extraction process. The results suggested that the octahedral-site is preferred for Na^+ insertion to form Na_xVS_2 with $0 < x \leq 1.0$. Afterwards, the intercalation occurs at the tetrahedral-site. In the first Na^+ insertion stage, S sites are play the role of redox center. While, in the second process, both V and S sites are related to redox procedures. 3.0 mol of Na^+ deep insertion leads to the conversion reactions to form metal V and Na_2S, which delivers a large theoretical specific capacity (699 mA h g^{-1}).

As another important member of TMCs, tin (IV) sulfide (SnS_2) with a typical layered structure is provided with a relative high theoretical specific capacity (1136 mA h g^{-1}), owing to the mixed alloying and conversion Na^+ storage mechanisms [146]. As we all know, the pseudocapacitance is significantly related to the exposed crystal planes of active materials [147]. Due to the anisotropy property of crystal structure, different exposed facets are predicted to hold different effects on the contribution of pseudocapacitive. Based on this idea, three kinds of SnS_2 nanosheets with gradually exposed different active facets were designed by our group [148]. As a result, different Na^+ storage performances and kinetics are generated accompanying with the morphology changes of SnS_2 nanosheets (Fig. 8a). In addition, the Na^+ storage mechanism of SnS_2 crystal structure is shown in Fig. 8b. Apparently, at the low rate, the fully charged crystalline SnS_2 can be achieved by both of the Na^+ intercalation and adsorption processes. With the increase of current rates, capacitive-controlled Na^+ storage process is gradually enhanced and dominant. As a result, lower the Na^+ diffusion energy barrier, as well as more stable active facets are of great importance for Na^+ storage, which can be achieved by reducing the size and thickness of nanosheets [148].

Tin(II) sulfide (SnS) is another kind of potential anode candidate for Na^+ storage on account of high electroconductivity, high specific capacity as well as small volume change accompanying with the repeated sodiation/desodiation processes. Chao and co-workers synthesized few-layered SnS nanosheets array straightly on the surface of graphene foam (GF), via a fast and low-temperature hot bath strategy [149]. The obtained SnS nanosheets present the thickness of 5 nm and the average lateral sizes of 50–70 nm (Fig. 7d). The sodium storage processes can be revealed by the followed CV tests (Fig. 8e). During the 1st discharge cycle, two obvious cathodic peaks located at ca. 0.65 and 0.01 V can be observed, where the peaks at ca. 0.6 V is related to the conversion and alloying processes (equation (14) and (15)), as well as the SEI formation [150]. In addition, another peak at ca. 0.01 V is assigned to the alloying process of Na and Na_xSn (x ~3.75). For the next charge cycle, some anodic peaks (~0.3, 0.7, 1.2–1.4 V) can be attributed to the step by step dealloying processes, moreover, an evident peak located at ca. 1.7 V responds to the followed conversion process resulting in SnS [151].

$$SnS + 2Na^+ + 2e\text{-} \rightleftharpoons Sn + Na_2S \quad (14)$$

$$4Sn + 15Na^+ + 15e^- \rightleftharpoons Na_{15}Sn_4 \quad (15)$$

The surface-controlled pseudocapacitance is regarded as the major Na^+ storage approach (Fig. 7c). On one hand, the structural stability and electronic/ionic conductivity can be achieved by the hybrid architecture. On the other hand, the mesoporous structure and ultrathin nanosheets guarantee the facilitated ion access and shortened ion diffusion. As a result, the SnS nanosheet structure possesses outstanding rate capability and superior specific capacity (~1100 mA h g^{-1} at 100 mA g^{-1}) than SnS nano-wall (~900 mA h g^{-1} at 100 mA g^{-1}) [149].

Ex-situ XRD analyses at various stages during the first charge/discharge process was performed by Cho and co-workers to further clarify the reaction mechanism of SnS, as shown in Fig. 8f [152]. The pristine diffraction pattern represents a typical orthorhombic SnS phase. After discharging to 0.65 V, the metallic Sn and Na_2S phases formed in the meantime, while the SnS phase disappeared completely, which corresponding to the conversion and alloying reactions of SnS. By discharging from 0.65 to 0.4 V, the peak intensity of Sn was increased and a c-$Na_{15}Sn_4$ phase was obtained, which indicates the conversion reaction is still occurring. After the completion of discharging to 0.01 V, the peak intensity of Sn phase becomes much weaker. After charging to 0.5 and 0.8 V, the two peaks belonged to Na_2S and $Na_{15}Sn_4$ are reduced, indicating the dealloying process. After charging to 1.2 V, the dealloying reaction was completed because the two peaks for Na_2S and $Na_{15}Sn_4$ disappeared completely. After the complete charging to 2.0 V, only peaks

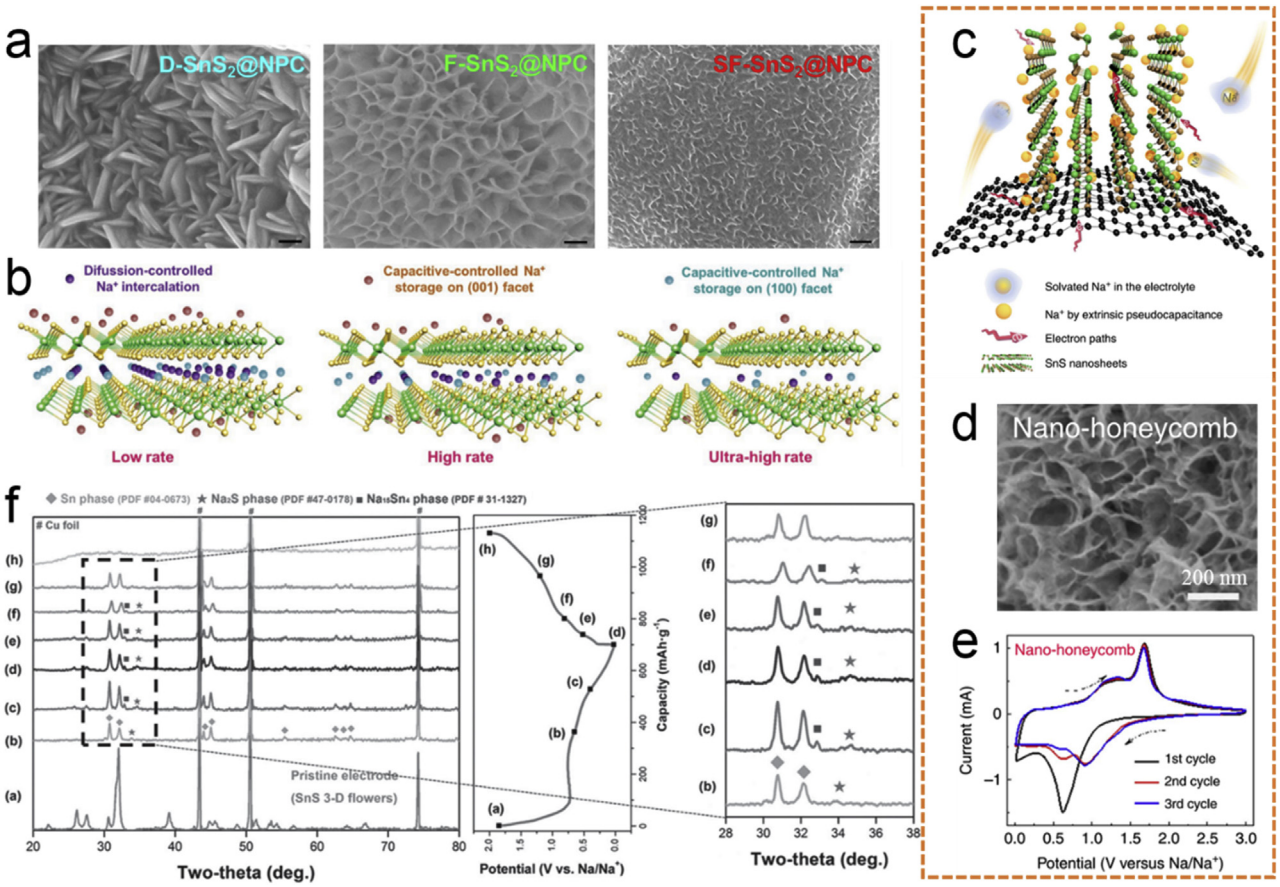

Fig. 8. (a) SEM images of the three kinds of SnS_2 nanosheets. (b) Schematic illustrating the Na^+ storage mechanism of SnS_2 crystal structure. Reprinted with permission from Ref. [148]. Copyright 2019, Wiley Online Library. (c) Schematic illustration of high-rate charge storage of SnS architecture. (d) SEM image of SnS nanosheets. (e) CV curves of the first three cycles of the SnS electrode. Reprinted with permission from Ref. [149]. Copyright 2016, Nature Publishing Group. (f) Ex-situ XRD patterns of the SnS 3D electrode at various charge/discharge stages. Reprinted with permission from Ref. [152]. Copyright 2018, Nature Publishing Group.

of Cu current collector are observed, which suggests the formation of amorphous or very small SnS [152].

3.3. Other type nanosheets

Carbon nanosheets (CCN) are universal materials used as the host of any Na-active material, such as Se. Ding and co-workers synthesized a carbon nanosheet matrix via hydrothermally treated and following KOH activation. Then, selenium was impregnated into carbon matrix through high-energy planetary co-milling followed by annealing under an argon atmosphere [153]. The obtained 3D architecture possesses high pore volume and good elasticity. In addition, as displayed in Fig. 9a, the decreased Na ion solid-state diffusion distances and the enhanced charge transfer can be obtained owing to the layered structure like other sheet-like materials. Moreover, the solvent molecules of EC and DMC with large dynamic sizes cannot penetrate to the CCN matrix, and the polyselenide formation and the shuttle effect can also be limited due to the absence of crystalline Se. The discharging profiles are illustrated on the right column of Fig. 9a. During discharging, Na^+ extracts from anode (i.e. $Na_xC \rightarrow x\ Na + C$), and reacts with Se to form Na_2Se [153].

To further improve the performance of Se–CCN, Yao and co-workers prepared a kind of free-standing and flexible Se/carbon hybrid material via encapsulating Se into nitrogen and oxygen dual-doped carbon interwoven by common carbon nanotube (CNT) (Se@NOPC-CNT) (Fig. 9b and c) [154]. The uniformly wrapped CNTs not only promote flexibility of the whole composite, but also provide conductive networks and paths for fast electronic/ionic transportation as well. Moreover, the doped porous carbon nanosheets enhance the chemical affinity and adhesion with Na_xSe ($0 < x \leq 2$). Thus, merits in these advantages, the obtained electrodes demonstrate outstanding Na^+ storage properties with high mass loading of Se (~60 wt%). The Coulombic efficiency remains nearly 100% even after 2000 cycles [154].

Yun and co-workers prepared graphene paper (ROGP) via a simple graphene oxide (G-O) modification strategy [155]. The as-obtained final product possesses good flexibility. The cross section SEM photographs illustrate a randomly oriented morphology of the ROGP, which is beneficial to the diffusion of Na^+ compared with the uniaxially oriented graphene electrode (Fig. 9d and e) [155].

Ternary tin thiophosphate (SnP_2S_6) with layered structure is another promising anode material for Na^+ storage. According to Fig. 9f, the interlayer distance is about 0.65 nm for the as-obtained layered SnP_2S_6. The intrinsic cation vacancies make the SnP_2S_6 possess internal polarity due to the asymmetric structure. The layered SnP_2S_6 holds the following advantages. First of all, the migration of ion or electron can be accelerated resulting from the internal electric fields of asymmetric SnP_2S_6, which is beneficial to improve electrochemical reaction dynamic [156]. In addition, easy Na^+ diffusion with low energy barrier can be guaranteed by the large interlayer spacing (~0.65 nm) of SnP_2S_6. Moreover, the ultrahigh theoretical capacity of ~1560 mA h g^{-1} makes SnP_2S_6 a prospective anode for SIBs. Furthermore, the charge transportation kinetics as well as rate capability are able to be further enhanced by the high conductivity discharge product of $Na_{15}Sn_4$ alloys. Liang and co-workers

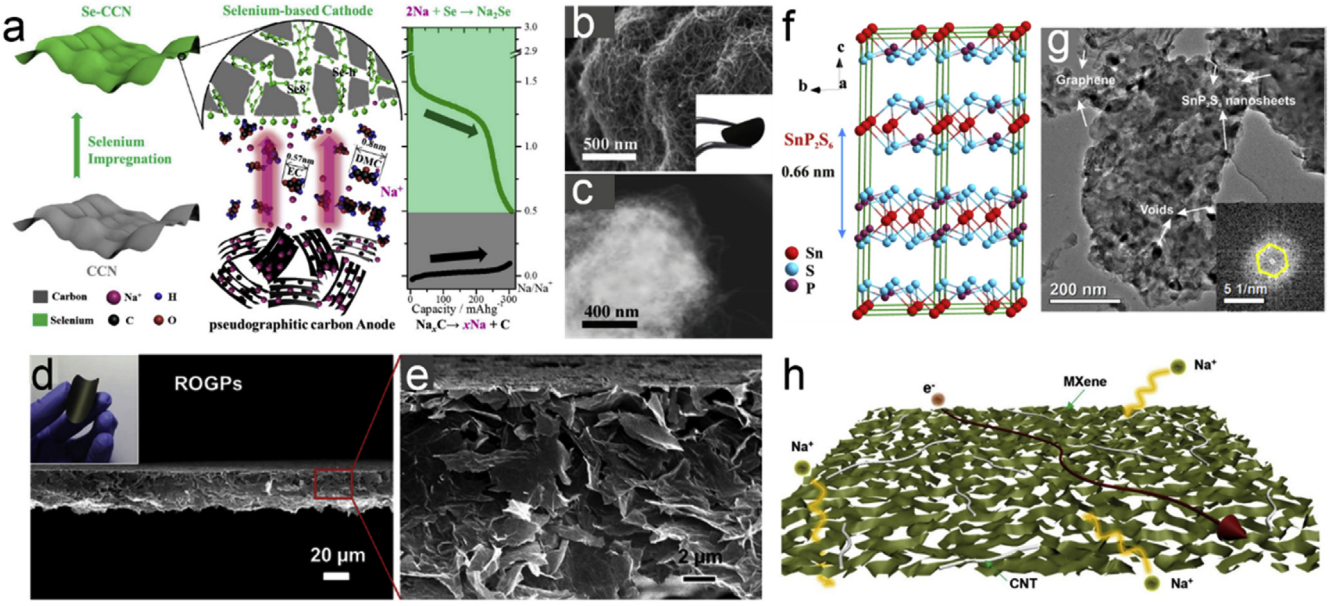

Fig. 9. (a) Schematic illustration and charge/discharge process of the Se–CCN electrode. Reprinted with permission from Ref. [153]. Copyright 2017, Royal Society of Chemistry. (b, c) SEM image and the dark-field image of Se@NOPC-CNT. Reprinted with permission from Ref. [154]. Copyright 2018, Wiley Online Library. (d, e) SEM images of the cross-sectional morphology of ROGP in different magnifications. Reprinted with permission from Ref. [155]. Copyright 2016, Elsevier. (f, g) Crystal model and TEM image of SnP_2S_6 nanosheets. Reprinted with permission from Ref. [157]. Copyright 2018, ACS Publications. (h) Na^+ diffusion and electron transfer within porous MXene/CNT electrodes. Reprinted with permission from Ref. [161]. Copyright 2016, Elsevier.

designed a novel 2D heterojunction with ultrathin SnP_2S_6 nanosheets onto the surface of graphene substrate (Fig. 9g) [157]. The Na^+ storage mechanisms of SnP_2S_6 are presented by the followed equations:

$$SnP_2S_6 + 21.75\ Na^+ + 21.75\ e^- \rightarrow 0.25\ Na_{15}Sn_4 + 2\ Na_3P + 6\ Na_2S \quad (16)$$

MXenes, 2D transition metal carbides, are formulated as $M_{n+1}X_nT_x$, in which M represents transition metal, such as Cr, Ti, Mo, V, Ta or Nb, and X means N and/or C, T represents the exterior termination O, F and/or –OH, and n is 1–3 [158,159]. Owing to the hydrophilicity and metallic conductivity, MXenes hold the potential for energy storage [160]. Based on the negative charge of MXene nanosheets as well as positive charge of CNTs, MXene/Carbon nanotube hybrid with porous structure was prepared via the electrostatic attraction [161]. As can be seen from Fig. 9h, the superior electrochemical performance of $Ti_3C_2T_x$/CNT-SA electrodes can be ascribed to these two major reasons. Firstly, the conductive $Ti_3C_2T_x$ nanosheets and CNTs can boost the transfer of electron in the electrode. Secondly, the inhibited restacking of MXene nanosheets can promote the transport of electrolyte as well as ion access into the anode [161]. Based the above-mentioned merits, the porous heterostructured MXene/CNT composite displays a high capacity (421 mA h cm^{-3}) and excellent cycling stability over 500 cycles.

Metal-organic frameworks (MOFs), a kind of hybrid organic-inorganic material with porous property, possess the advantages of regular ion diffusion pathways, controllable chemistry and functionality, as well as abundant active sites [162–164]. Li and co-workers synthesize nanosheets based on Co(II)-terephthalate MOF (named "u-CoOHtp") via a facile ultrasonic method [165]. Because of the unsaturated sites possessed by the exposed material surfaces, oxygen vacancies were created, which would improve the rates of Na^+ diffusion and transportation. The mechanism of Na^+ intercalation/extraction was proposed. In the discharging process, the Co^{2+} is reduced to Co^0 under the voltage larger than 0.4 V. Afterwards, extra Na ions are stored by the O atoms provided by carboxyl to the end. In the charging procedure, Na^+ firstly extracts from carboxyl oxygen atoms under the voltage below 1.1 V, and then Co^0 is oxidized to Co^{2+} [165].

In addition to the above substances, other kinds of nanosheet materials, such as layered double hydroxides [166], bismuthene [167], and sodium birnessite [168,169] are also explored. Since these materials are relatively not general, a brief introduction about these materials is discussed here. Due to the generated crystal water in the interlayer space and the solid solution of two transition metals, the crystal structure of layered double hydroxide can be stabilized, thus exhibits fast charge/-discharge operation [170]. Bismuth, with the advantages of nontoxic, high electronic conductivity as well as chemical properties, is regarded as a very promising anode material [171]. The large interlayer spacing of 3.979 Å can significantly facilitate the diffusion of Na^+. A high areal sodium storage capacity of 12.1 mA h cm^{-2} can be obtained based on bismuth electrodes [172]. Sodium birnessite with a relatively large interlayer distance of about 7 Å can promote the fast migration of Na^+ and enhance the structural stability, thus achieve large specific capacity (211.9 mA h g^{-1}), outstanding cycle performance (1000 cycles), and excellent rate capability (156.0 mA h g^{-1} at 50C) [173].

4. Nanosheet-based materials for rechargeable multivalent battery systems

In recent years, portable electronic devices, electric vehicle and scale energy storage have been greatly developed, thus using various approaches to increase energy densities of battery systems becomes a hot topic for researchers all over the world [172]. However, material level enhancements of LIBs are approaching to the theoretical maximum, and as a result, attempts to developing new and beyond battery systems which can offer a remarkable energy density improvement as well as reduce the cost are becoming indispensable. Multivalent (MV) chemistries (Mg^{2+}, Zn^{2+}, and Al^{3+}) and rechargeable multivalent batteries (MIBs, ZIBs, AIBs) hold the potential to meet the aforementioned requirements, since multivalent positive ion can deliver two or three electrons per ion [173]. Multivalent cations can provide more capacity than Li^+ if occupying a similar number of insertion sites when inserted into a cathode material [173,174].

MIBs have been regarded as one of the potential candidates to build an electrochemical energy system secure as well as high density. MIBs hold the following advantages. First of all, the Mg content in nature is abundant, and they are intrinsically stable under the atmosphere of air

[175]. In addition, Mg anode delivers a high theoretical capacity (2205 mA h g^{-1} or 3833 mA h cm^{-3}), and a nearly 100% efficiency due to its bivalency [176]. Furthermore, it is safe to use the magnesium anode because no dendrites will be formed [173], which is one of the obvious advantages compared with Li metal batteries. Unfortunately, the development of MIBs has been hindered by the cathode materials due to the low transportation kinetics of magnesium ions caused by the double charge density of Mg^{2+} [177]. A method to solve the above constraint is to build a Mg/Li hybrid battery system, using Mg based anode, Li based cathode as well as mixed electrolyte of Mg^{2+}/Li^{+} [178,179]. This approach use kinetically more efficient Li^{+} to replace kinetically sluggish Mg^{2+} intercalation/deintercalation, thus can achieve a satisfactory capacity and energy/power densities. Another solution is introducing 2D nanosheet materials with expanded interlayer spacing and a weaker Coulombic attraction with guest Mg^{2+} ions to MIBs. The weaker Coulombic attraction can enhance the mobility of Mg^{2+}, as well as the desolvation of Mg^{2+} at the electrolyte/electrode interface.

Different from nonaqueous organic solvents mostly used in other secondary batteries, the aqueous ZIBs utilized Zn metal anode and water-based electrolytes, which have outstanding prospects for large-scale energy storage [174]. Zn metal has plentiful resource and is low-cost and stable. Moreover, Zn anode holds a significantly high theoretical capacity of 820 mA h g^{-1} [180]. In addition, aqueous electrolyte provides higher electrical conductivity and lower toxicity compared with organic electrolyte [174]. However, the intercalation chemical process of zinc ions which limited by inherent characteristic was hindered the further development of ZIBs. Divalent Zn^{2+} generally shows high electrostatic tenacity to interactive with host lattice, which can lead to slow Zn^{2+} diffusion, thereby inhibiting reversibility of intercalation [181]. Thus, find new strategies to design and synthetic materials where Zn^{2+} can intercalate reversibly are required.

AIBs are another kind of rechargeable multivalent batteries systems, which possess its unique advantages. The highest multivalent charge carrier (Al^{3+}) is able to offer high gravimetric/volumetric of 2980 mA h g^{-1}/8046 mA h cm^{-3} [182]. Unfortunately, the strong polarization effect which arises from the large charge density of multivalent cations can destroy local electrical neutrality and collapse the crystal lattice as well as decrease electrochemical performances [174]. In addition, the large ionic group chloroaluminate anion ($AlCl_4^-$, another kind of inserted ions in AIBs), which is difficult to intercalate into cathode, lead to the negative effect in capacity and cycling stability of electrode [174]. Therefore, how to develop the electrode materials with a weaker coulombic attraction with Al^{3+} and achieve the reversible insertion\extraction of Al^{3+} are attracting the wide attention.

4.1. TMOs nanosheets

VO_2 have received much attention in the energy storage applications due to its unique characteristics of outstanding structural flexibility and low-toxicity [183]. Monoclinic VO_2 (B) is a kind of layered material assembled by edge-shared VO_6 octahedrons. This structure formed the corner-shared connections between the adjacent cells, thus generate V–O tunnels, which can provide an accommodation for a different kind of guest ions like Mg^{2+} [184]. Luo and co-workers synthesized VO_2 (B) nanosheets via a simple hydrothermal approach for using as the cathode for Mg ion batteries (Fig. 10a) [185]. To explore the mechanism of Mg^{2+} storage, charge/discharge curves between −1.0 V and 0.3 V was performed, which revealed that VO_2 (B) only have one oblique discharge platform at ca. 2.15 V vs. Mg^{2+}/Mg (Fig. 10b). Moreover, As can be seen from Fig. 10c, the VO_2 (B) nanosheets are potentially separated at 0.05 V, suggesting rapid kinetics as well as high reversibility of VO_2 (B) nanosheets during Mg^{2+} insertion/deinsertion process. The Mg^{2+} storage mechanism can be summarized as $VO_2 + x\ Mg^{2+} + 2\times\ e^- \rightarrow Mg_xVO_2$ [185].

Zhao and co-workers prepared the MnO_2 nanostructure via the electrodeposition method [186]. The size and thickness of the obtained

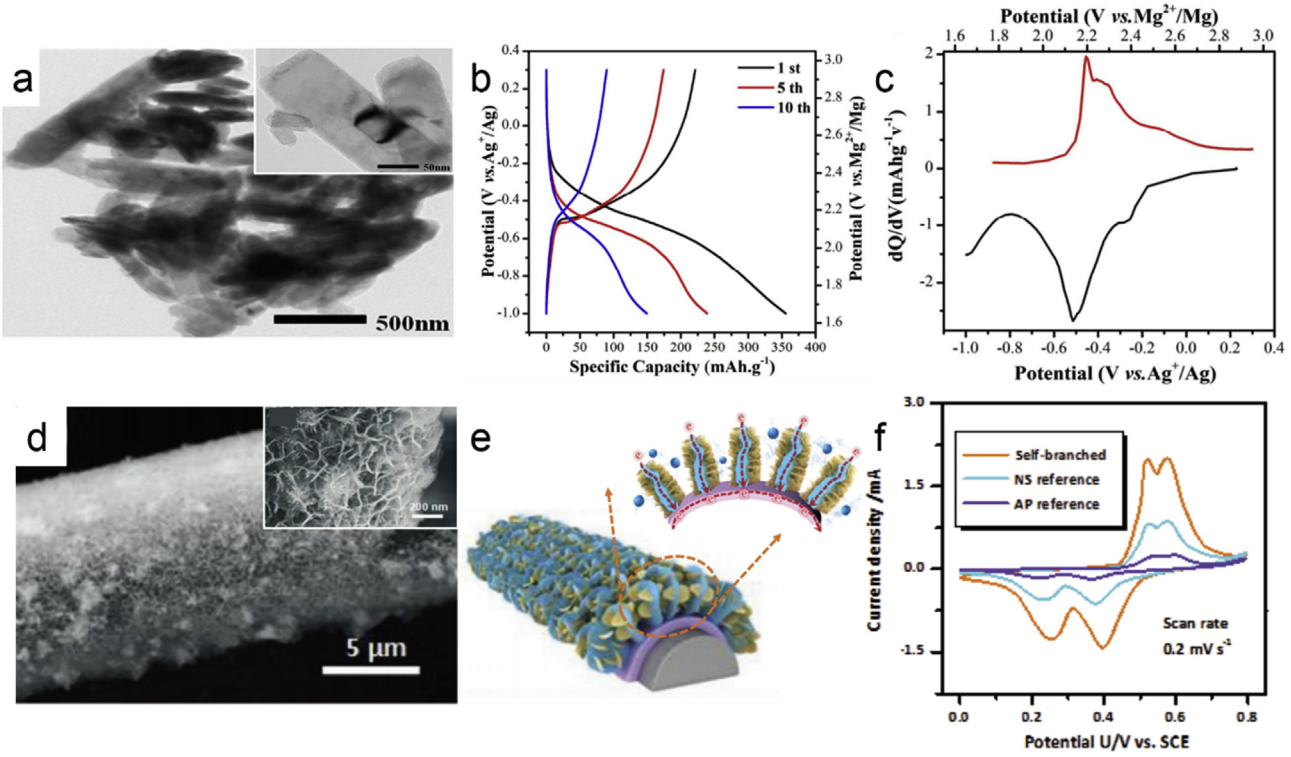

Fig. 10. (a) Morphology characterization of VO_2 (B) nanosheets. (b, c) The charge/discharge and dQ/dV curves for VO_2 (B) nanosheets. Reprinted with permission from Ref. [185]. Copyright 2018, Elsevier. (d) SEM images of the self-branched hierarchical structure of MnO_2. (e) Schematic illustration of electrons and ions transport within the electrode. (f) CV curves of hierarchical MnO_2electrode. Reprinted with permission from Ref. [186]. Copyright 2018, Wiley Online Library.

solitary nanosheets are respectively 200–300 nm and 20–30 nm. All of the nanosheets are vertically aligned on the fiber, composing a surface which covered with uniformly crossed network textile fiber, which can not only facilitate the quick ion diffusion, but promote the electrode stability during the cycles. To further enhance the energy storage capability, large number of smaller fluffy nanosheets (5–10 nm) were introduced to the bulk nanosheet array, lead to a self-branched hierarchical structure (Fig. 10d). Such unique structure can not only build numerous networks but offer more favorable paths for rapid ion diffusion as well, which is beneficial for promoting the rate performance (Fig. 10e). In addition, the mass loading of MnO_2 nanosheets is greatly enhanced from 3.96 mg cm^{-2} to 9.15 mg cm^{-2}, which can be ascribed to the introduction of fluffy nanosheets. To investigate the mechanism of Zn storage, the charge/discharge curves is performed (Fig. 10f). The related CV peaks suggests the multi-step H^+ and Zn^{2+} storage in MnO_2 [187]. Cycling performance shows that 91% of the capacity was retained at 1C even after 1000 cycles, exhibiting the outstanding long cycle life of the as-prepared MnO_2 nanosheet-based electrode [186].

4.2. TMCs nanosheets

TMCs have attracted intensive attention owing to the layered structures integrated by vdW interactions, which is beneficial for the guest molecules and/or ions to intercalate into layers [188]. Due to the large interlayer spacing of 0.62 nm, MoS_2 were broadly used for Li^+/Na^+ battery anode as well as other various multivalent batteries system [189]. MoS_2 nanosheets with expanded interlayer on graphene foam (E-MG) was synthesized by Fan and co-workers via a hydrothermal reaction followed by thermal treatment method as cathodes for MIBs (Fig. 11a and b) [190]. The interlayer was expanded to 1.00 nm, which not only decrease Mg^{2+} diffusion barrier, but also improve the structural stability during Mg^{2+} intercalation (Fig. 11c). CV of MoS_2 electrodes was performed to further investigate the mechanism of Mg storage (Fig. 11d). Two remarkable pairs redox peaks of 0.92/1.19 V and 1.02/1.25 V are detected. Cycling performance displays that after 200 cycles, 81% of the capacity was remained at 500 mA g^{-1} with nearly 100% columbic efficiency (Fig. 11e), which reveals a stable cycling performance and an enhanced performance than bulk MoS_2 owing to the rich active sites and shorten ion diffusion pathways caused by nanosheet structure [190]. A slight expansion of interlayer distance was observed after prolonged cycles, which may be attributed to the self-adjusting of the structure to make more Mg^{2+} intercalate into the MoS_2 layers.

In order to boost divalent-ion storage capacity, defect chemistry was introduced to the MoS_2 nanosheets for ZIBs [191]. Defect engineered MoS_{2-x} nanosheets was synthesized by Xu and co-workers (Fig. 11f) [181]. DFT calculations revealed that the sulfur vacancies and edges of the MoS_2 nanosheets are the major adsorption sites of Zn^{2+}, and it also can generate pseudocapacitance of the MoS_2 cathode. For the purpose of further explore Zn^{2+} storage mechanism of the MoS_2 electrodes, CVs are performed at different scan rates. With a relative slow scan rate (0.1 mV s^{-1}), the electrochemical reactions are mainly controlled by the diffusion process. While, the contribution of the capacitive processes is increased along with the improving scan rate (Fig. 11g). The ex-situ XPS was also carried out to analyses the Zn^{2+} storage mechanisms of defected MoS_2. A High-resolution ex-situ Mo (VI) $3d_{3/2}$ spectra during charge/-discharge process is further analyzed. The peak intensity of Mo (VI) $3d_{3/2}$ decreased progressively during the first discharge process from initial voltage to 0.25 V, which revealed the gradual reduction of the Mo valance state. While, the peak intensity of Mo (VI) $3d_{3/2}$ progressively strengthened to its initial state when charged from 0.25 to 1.25 V, which suggested the rebirth of Mo (VI) (Fig. 11h–j). The electrochemical reactions of the MoS_2/Zn battery are concluded as follows:

$$\text{Cathode: } MoS_{2-x} + 0.36\ Zn^{2+} + 0.728\ e^- = Zn_{0.36}MoS_{2-x} \quad (17)$$

$$\text{Anode: } Zn^{2+} + 2e^- = Zn \quad (18)$$

Electrochemical performance shows that the defect-rich MoS_2 nanosheets exhibits a starting capacity of 100.9 mA h g^{-1} and a capacity reservation of 87.8% over 1000 cycles at 1000 mA g^{-1} [181].

Due to the instinct metallic electronic ground state, VS_2 holds a propitious future for the applications of energy storage. Meng and co-workers synthesized VS_2 nanosheetsfor MIB cathodes through hydrothermal route. The diameter and thickness of the as-prepared nanosheets are around 500 and 50 nm [179]. Combined XRD, TEM analysis and theoretical calculation exposed that the interlayer spacing of VS_2 can be expanded to 8.76 Å because of the insertion of $(phenyl)_2Mg$ and tetrahydrofuran at the early cycling stage. As a result, it reaches maximum energy and power densities of 231 W h kg^{-1} and 5722 W kg^{-1}. CV curve indicates that the capacity is dominated by pseudo-capacitance [179].

4.3. Other type nanosheets

$VOPO_4$, as polyanion-type layered materials, exhibits architecture of corner-sharing VO_6 octahedra connected to PO_4 tetrahedra [192]. Owing to the five-coordination circumstance of vanadium ion, the vacant coordination sites between the restacking layers can provide cation intercalation. Zhou and co-workers synthesized $VOPO_4$ nanosheets with expanded layer spacing via a facile ultrasonicated exfoliation and self-assembly strategy [193]. The layer spacing of nanosheets is expanded from 0.74 to 1.42 nm through a displacement reaction with phenylamine (PA) molecules. Combined experimental evidence with calculations, the expanded $VOPO_4$ nanosheets can afford sufficient interlayer spacing to absorb $MgCl^+$, and further improve the diffusion dynamics (Fig. 12a). A high reversible capacity of 310 mA h g^{-1} and cycle stability of 192 mA h g^{-1} for 500 cycles can be achieved [193].

Spinel nickel cobaltite ($NiCo_2O_4$) is a potential candidate for LIBs and supercapacitors (SCs) due to its superior electrical conductivity and electrochemical activity [194]. Zeng and co-workers synthesized oxygen vacancies and surface phosphate ions enriched ultrathin nickel cobaltite ($NiCo_2O_4$) nanosheets via annealing the pristine $NiCo_2O_4$ nanosheets using a facile phosphating strategy [180]. On one hand, oxygen vacancies enhance the conductivity of metal oxide, as well as serve as active sites for electrochemical reactions. On the other hand, the surface reactivity and reaction kinetics can be greatly improved by the introduced phosphate ion. To figure out the electrochemical mechanism of the $NiCo_2O_4$ electrode, CV curves are measured, and the linear relationship between i and $\nu^{1/2}$ shows the redox reaction is a diffusion-controlled process (Fig. 12b). The electrochemical reaction of the $NiCo_2O_4$/Zn battery is concluded as follows [195].

$$\text{Cathode: } NiCo_2O_4 + OH^- + H_2O \rightleftharpoons NiOOH + 2\ CoOOH + e^- \quad (19)$$

$$CoOOH + OH^- \rightleftharpoons CoO_2 + H_2O + e^- \quad (20)$$

$$\text{Anode: } [Zn(OH)_4]^{2-} + 2\ e^- \rightleftharpoons Zn + 4\ OH^- \quad (21)$$

Electrochemical performance test result exhibits remarkable energy and power densities of 616.5 W h kg^{-1} and 5.15 kW kg^{-1} [180].

A 3D hierarchical nanosheet-based microsphere AlV_3O_9 was prepared by a simple hydrothermal route (Fig. 12c). Ex-situ XRD analysis was performed to reveal the Al^{3+} storage mechanism (Fig. 12d). As the discharging process progresses, the peak of Al_2O_3 is gradually increased, indicating the conversion reaction of Al^{3+} inserting in the AlV_3O_9 electrode. While, along with the charging process, the peak of Al_2O_3 is progressively decreased, suggesting the extraction of Al^{3+} from the electrode and the regeneration of AlV_3O_9. Such a result indicates that AlV_3O_9 can achieve reversibe intercalation and de-intercalates of Al^{3+}, and phase transition takes place at the interface of electrode material [196]. The electrochemical reaction can be concluded as follows:

$$\text{Cathode: } AlV_3O_9 + x\ Al^{3+} \rightleftharpoons Al_{3+x-y}V_3O_{9-1.5y} + 0.5y\ Al_2O_3 + 3\times\ e^- \quad (22)$$

$$\text{Anode: } Al + 7\ AlCl_4^- \rightleftharpoons 4\ Al_2Cl_7^- + 3\ e^- \quad (23)$$

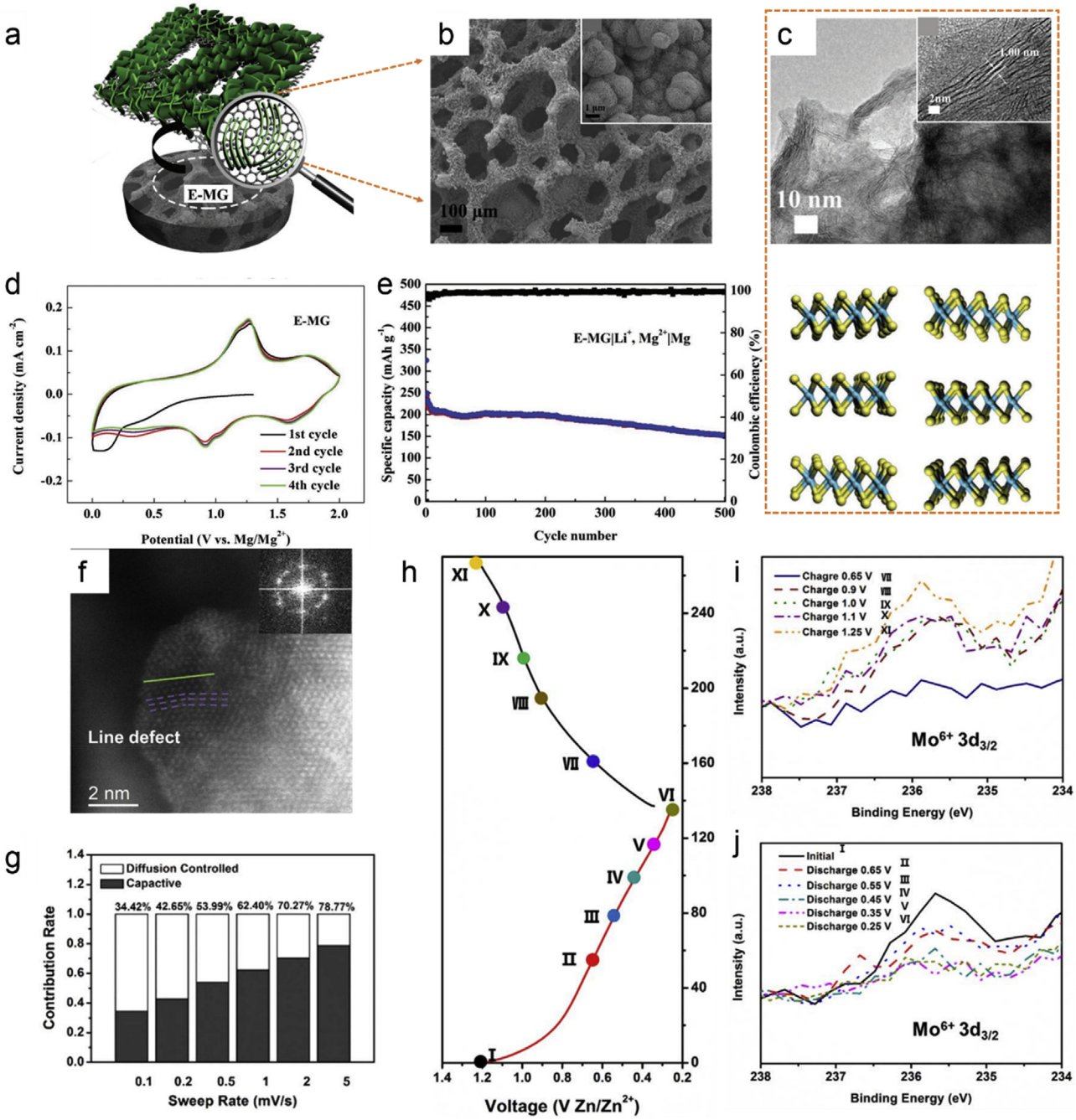

Fig. 11. (a, b) Schematic and SEM image of E-MG. (c) HRTEM images and structure model of E-MG. (d, e) CV curves and cycle stability of E-MG. Reprinted with permission from Ref. [190]. Copyright 2017, Wiley Online Library. (f) STEM image defect-rich MoS_2 nanosheets. (g) The contribution ratio of the capacitive capacities and diffusion-limited capacities. (h) Initial charge/discharge curve of MoS_2 electrode at 100 mA g^{-1}. (i, j) Ex-situ Mo^{6+} 3d$_{3/2}$ spectra and Mo 3d spectra of MoS_2 electrode at different states. Reprinted with permission from Ref. [181]. Copyright 2019, Elsevier.

Electrochemical performance shows that a high discharge specific capacity of 327 mA h g^{-1} can be achieved at 100 mA g^{-1} [196].

Xie and co-workers synthesized a fluorinated graphene nanosheet (FGS) network for MIBs via a hydrothermal fluorination procedure, and after a anionic insertion process resulting in pre-activation for FGS [197]. The electrochemical mechanism of the Mg/FGS battery system was investigated through XPS analysis, and the results revealed that there are three separated reaction stages before reaching the reversible state of the whole battery system (Fig. 12e). After the first a few cycles, the electrochemical reactions at cathode side can be summarized as follows:

$$\text{C-X(X = F,Cl,ClO}_4\text{)} + \text{Mg(DMSO)}_n\text{ClO}_4^+ + 2\,e^- \rightleftharpoons \text{Mg-X-C} + \text{n(DMSO)} + \text{ClO}_4^- \quad (24)$$

$$\text{C-X} + \text{MgCl}^+ + 2\,e^- \rightleftharpoons \text{Mg-X-C} + \text{Cl}^- \quad (25)$$

$$2\,\text{C-X} + \text{Mg}_2\text{Cl}_3^+ + 4\,e^- \rightleftharpoons 2\,\text{Mg-X-C} + 3\,\text{Cl}^- \quad (26)$$

and at anode side by:

$$\text{Mg(DMSO)}_n\text{ClO}_4^+ + 2\,e^- \rightleftharpoons \text{Mg} + \text{n(DMSO)} + \text{ClO}_4^- \quad (27)$$

$$\text{MgCl}^+ + 2\,e^- \rightleftharpoons \text{Mg} + \text{Cl}^- \quad (28)$$

$$\text{Mg}_2\text{Cl}_3^+ + 4\,e^- \rightleftharpoons 2\,\text{Mg} + 3\,\text{Cl}^- \quad (29)$$

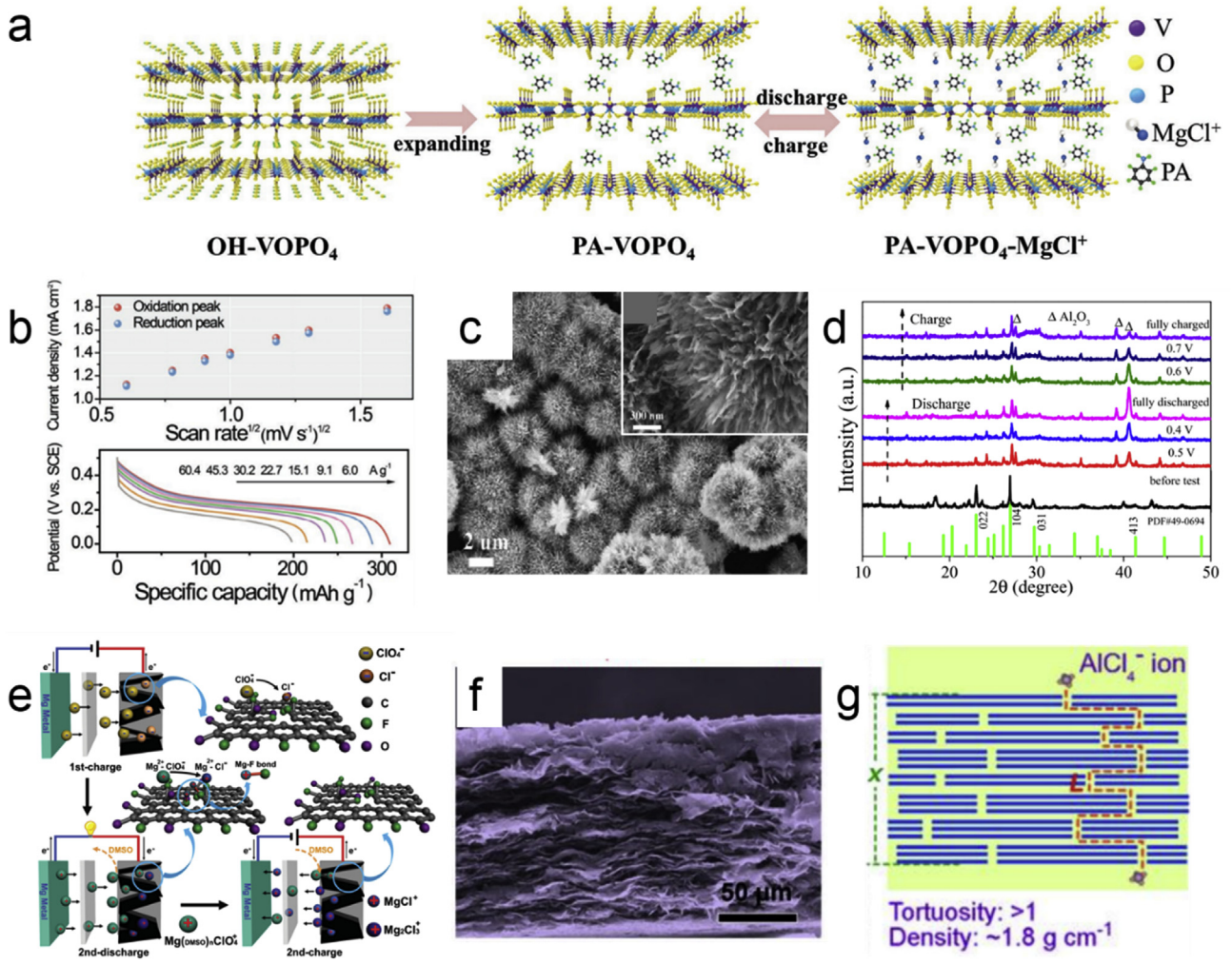

Fig. 12. (a) Schematic illustration of the proposed mechanism of expanded $VOPO_4$ nanosheets. Reprinted with permission from Ref. [193]. Copyright 2018, Wiley Online Library. (b) Variation in the redox peak currents with the square root of the scan rates, and discharge curves at various current densities. Reprinted with permission from Ref. [180]. Copyright 2018, Wiley Online Library. (c) SEM images of AlV_3O_9. (d) Ex-situ X-ray diffraction pattern of AlV_3O_9 electrode. Reprinted with permission from Ref. [196]. Copyright 2019, Elsevier. (e) Schematic illustration of electrochemical mechanisms of the Mg/FGS battery system. Reprinted with permission from Ref. [197]. Copyright 2015, Wiley Online Library. (f) Cross-sectional SEM view of GN papers. (g) Schematic illustration of cross-sectional features for understanding the tortuosity of the ion transport in the electrode. Reprinted with permission from Ref. [198]. Copyright 2018, Elsevier.

Electrochemical performance shows a stable cycling life and rate performance with capacities of 110, 90 and 50 mA h g^{-1} at 10, 50 and 100 mA g^{-1}, respectively [197].

Wang and co-workers prepared graphene nanosheet (GN) papers and introduced it as an host material for fast $AlCl_4^-$ ion transfer/storage [198]. Morphology characterization suggests that the GN papers were combined with significantly thinner and smaller nanosheests (Fig. 12f), which holds the advantages of abundant ionic diffusion pathways, decreased ion transport distances as well as enhanced cushion areas for $AlCl_4^-$ diffusion/storage. Moreover, such stacked graphene nanosheets with moderate tortuosity can balance the application of the every active material unit with highly effective transportation paths, which is of vital importance to volumetric energy and power density (Fig. 12g) [198]. The electrochemical mechanismcan be concluded as follows:

$$\text{Cathode: } C_n + AlCl_4^- \rightleftharpoons C_n[AlCl_4] + e^- \quad (30)$$

$$\text{Anode: } Al + 7\ AlCl_4^- \rightleftharpoons 2\ Al_2Cl_7^- + 3e^- \quad (31)$$

The GN cathode delivered an extremely high volumetric capacity of 170 mA h cm^{-3} at 50 mA g^{-1} along with the volumetric energy and power densities of 0.2774 Wh cm^{-3} and 10.9122 W cm^{-3}, which is closes to the theoretic values [198].

5. Nanosheet-based materials for next-generation Li batteries

Owing to the increasing requirements of high energy and high power density, next-generation Li batteries, such as Li-sulfur (Li–S) and Li-air batteries, have attracted intensive attention of researchers [199–202]. Unfortunately, the shuttling of soluble Li polysulfides (Li_2S_x, $2 \leq x \leq 8$) leads to low Coulombic efficiency, continuous loss of active materials, as well as severe decay of capacity and cycling life. Therefore, how to regulate the transportation and kinetics behaviors of Li_2S_x is a critical problem [203]. Introducing polar transition metal compounds, such TMCs, is regarded as an effective strategy to relieve the above drawback, and achieve improved electrochemical performances. Here, we will make a brief introduction on these projects.

One way to address the "shuttle effect" is to introduce compounds with strong adsorption ability to capture the polysulfides. It is widely accepted that a moderate binding energies with polysulfides in the range of 0.8–2.0 eV is an important feature for the coupling materials. Based on this, Yao and co-workers synthesized antimony sulfides (Sb_2S_3) nanosheets via electrochemical Li intercalation and followed by exfoliation of

Sb_2S_3 [204]. Based on the DFT calculations, the obtained nanosheets are proved to display ideal binding energies ranging from 1.33 to 2.14 eV, and hold the low-energy barrier (189 meV) for Li diffusion. Combining with the conductive CNT network, the modified Li–S cell illustrates an enhanced capacity with a limited decay rate for over 200 cycles.

Vanadium nitride (VN) nanosheets are also investigated to relieve the shuttling of polysulfides [205]. Due to the strong polar-polar chemical interaction between VN and polysulfides, the loss of active materials is obviously reduced. Combined with the "physical block" provided by the porous carbon fibers (PCF), the designed PCF/VN/S electrode delivers excellent performance (1310.8 mA h g^{-1} at 0.1C) and prolonged cycle life.

As a kind of typical 2D layered material, graphene has attracted considerable attention in energy storage fields due to its high surface-volume ratios and abundant active binding sites. Shi and co-works designed a nitrogen-doped graphene skin deposited on the surface of graphene framework for Li–S batteries [206]. The fully exposed N heteroatoms can act as the anchoring sites of polysulfide to achieve high sulfur utilization, thus resulting in enhanced cyclic stability (1039 mA h g^{-1} at 1.0C, 0.09% decay per cycle). Recently, researchers have developed many novel approaches to synthesize doped graphene materials. Kong and co-workers have developed a facile method to synthesize nitrogen-dopant carbon nanosheets via pyrolyzing a thin layer of 2D porphyrin organic framework on the surface of graphene, resulting in improved Li–S cell performances (1135 mA h g^{-1} at 0.5C, 0.099% decay per cycle) [207].

Another effective way to relieve the "shuttle effect" is to shorten the existence time of polysulfides through accelerating the conversion of soluble polysulfides. Therefore, compounds with excellent electrochemical catalytic ability for polysulfides have attracted intensive attention. Li and co-workers synthesized ultra-thin Fe_3C nanosheets on mesoporous carbon as the multifunctional sulfur host [208]. The Fe_3C nanosheets can act as the active sites to capture polysulfides, as well as catalytic sites to transform soluble polysulfides. Combined with conductive mesoporous carbon, the sulfur host can boost the transportation of electrons and ions, lock polysulfides, as well as enhance the reaction kinetics. Therefore, the designed multifunctional sulfur host exhibits a high capacity of 1530 mA h g^{-1} at the current density of 0.1C.

6. Conclusions and outlook

This review provides a comprehensive introduction of recent nanosheet-based electrode materials for high performance batteries, like LIBs, SIBs, MIBs, ZIBs, AIBs, and various kinds of energy storage mechanisms are discussed and summarized meanwhile. Owing to the short solid-state diffusion distance for ions, the ability to alleviate the huge volume expansion of the electrode during repeated charge/discharge process, large numbers of channels for the access of electrolyte to improve the speed of ions diffusion within the electrode, as well as the numerous exposed active sites, nanosheet-based electrode materials have attracted intensive attention and have been studied in recent years for achieving ultrafast charge/discharge of energy storage. Furthermore, the defect engineering, heterostructure configuration, as well as doping can further improve the electrochemical performance of various nanosheet-based electrodes. Although nanosheet-based electrode materials provide an opportunity for achieving ultrafast charging and discharging of different battery systems, a large amount of effort is still needed to achieve the expected goal. In order to further realize the practical applications of nanosheet-based materials, the key challenges and some perspectives are summarized as follows.

(1) The traditional synthetic strategies of TMOs are relatively complex and not general, as well as not environmentally friendly [209]. Thus, synthesis methods with controllable, effective and large-scale characteristics are expected to be developed. Moreover, the understanding of energy storage mechanisms, especially in multivalent rechargeable battery systems, should be investigated via advanced characterization methods, such as in-situ XRD/Raman/XPS technologies.

(2) For TMCs, the main limitations are poor electronic conductivity, strong restacking and aggregation tendency, as well as unignorable volume variation during repeated charge/discharge processes. As a result, combining with conductive materials (such as carbonaceous nanotubes and sheets), and exploring effective strategies to expand the layer distance are vital to improve their capabilities of ion storage.

(3) Although 2D graphene, silicene, BP and MXene hold many advantages for ion storage, there still exist some difficulties to achieve their further applications, such as the tendency of restacking and aggregation, as well as the lack of suitable methods for large-scale preparation of high quality BP [210]. Therefore, exploring strategies to solve these problems are of vital importance. Expanding the layer distance to hinder the restacking, introduction of defects and heterogeneous, as well as construction the 3D network structures are considered to be effective solutions to address the above difficulties and enhance their electrochemical performances. What's more, exploring low cost and non-toxic preparation methods for high quality BP is also imperative.

With rapid development and constantly exploring in materials design and engineering, we hold the view that nanosheet-based electrode materials can boost the development of rechargeable batteries and bring a bright future of energy storage science and technology.

Declaration of competing interest

There are no conflicts of interest to declare.

Acknowledgements

This work was mainly supported by MoE Tier 1 (Grant No. RG19/17). W. H. thanks the supports by the National Basic Research Program of China-Fundamental Studies of Perovskite Solar Cells (Grant No. 2015CB932200), Natural Science Foundation of Jiangsu Province (Grant No. BM2012010), Priority Academic Program Development of Jiangsu Higher Education Institutions (Grant No. YX03001), Ministry of Education of China (Grant No. IRT1148), Synergetic Innovation Center for Organic Electronics and Information Displays, and the National Natural Science Foundation of China (Grant Nos. 61136003 and 51173081).

References

[1] G. Chen, L.T. Yan, H.M. Luo, S.j. Guo, Nanoscale engineering of heterostructured anode materials for boosting lithium-ion storage, Adv. Mater. 28 (2016) 7580–7602.
[2] S. Chu, A. Majumdar, Opportunities and challenges for a sustainable energy future, Nature 488 (2012) 294–303.
[3] A.S. Arico, P. Bruce, B. Scrosati, J.M. Tarascon, W.V. Schalkwijk, Nanostructured materials for advanced energy conversion and storage devices, Nat. Mater. 4 (2005) 148–159.
[4] H.G. Zhang, X.D. Yu, P.V. Braun, Three-dimensional bicontinuous ultrafast-charge and -discharge bulk battery electrodes, Nat. Nanotechnol. 6 (2011) 277–281.
[5] P.G. Bruce, B. Scrosati, J.M. Tarascon, Nanomaterials for rechargeable lithium batteries, Angew. Chem. Int. Ed. 47 (2008) 2930–2946.
[6] C.M. Doherty, R.A. Caruso, B.M. Smarsly, P. Adelhelm, C.J. Drummond, Hierarchically porous monolithic $LiFePO_4$/carbon composite electrode materials for high power lithium ion batteries, Chem. Mater. 21 (2009) 5300–5306.
[7] L.F. Cui, Y. Yang, C.M. Hsu, Y. Cui, Carbon-silicon core-shell nanowires as high capacity electrode for lithium ion batteries, Nano Lett. 9 (2009) 3370–3374.
[8] A. Magasinski, P. Dixon, B. Hertzberg, A. Kvit, J. Ayala, G. Yushin, High-performance lithium-ion anodes using a hierarchical bottom-up approach, Nat. Mater. 9 (2010) 353–358.
[9] H. Wu, G. Chan, J.W. Choi, I. Ryu, Y. Yao, M.T. McDowell, S.W. Lee, A. Jackson, Y. Yang, L.B. Hu, Y. Cui, Stable cycling of double-walled silicon nanotube battery anodes through solid–electrolyte interphase control, Nat. Nanotechnol. 7 (2012) 310–315.
[10] C.K. Chan, H. Peng, G. Liu, K. Mcilwrath, X.F. Zhang, R.A. Huggins, Y. Cui, High-performance lithium battery anodes using silicon nanowires, Nat. Nanotechnol. 3 (2008) 31–35.

[11] S.B. Yang, Y. Sun, L. Chen, Y. Hernandez, X.L. Feng, K. Mullen, Porous iron oxide ribbons grown on graphene for high-performance lithium storage, Sci. Rep. 2 (2012) 427.

[12] H.L. Wang, L.F. Cui, Y. Yang, H.S. Casalongue, J.T. Robinson, Y.Y. Liang, Y. Cui, H.J. Dai, Mn_3O_4-graphene hybrid as a high-capacity anode material for lithium ion batteries, J. Am. Chem. Soc. 132 (2010) 13978–13980.

[13] D. Zhang, S. Wang, Y. Ma, S.B. Yang, Two-dimensional nanosheets as building blocks to construct three-dimensional structures for lithium storage, J. Energy Chem. 27 (2018) 128–145.

[14] S.B. Yang, Y.J. Gong, Z. Liu, L. Zhan, D.P. Hashim, L.L. Ma, R. Vajtai, P.M. Ajayan, Bottom-up approach toward single-crystalline VO_2-graphene ribbons as cathodes for ultrafast lithium storage, Nano Lett. 13 (2013) 1596–1601.

[15] T. Sasaki, M. Watanabe, H. Hashizume, H. Yamada, H. Nakazawa, Macromolecule-like aspects for a colloidal suspension of an exfoliated titanate. Pairwise association of nanosheets and dynamic reassembling process initiated from it, J. Am. Chem. Soc. 118 (1996) 8329–8335.

[16] J. Mei, T. Liao, L.Z. Kou, Z.Q. Sun, Two-dimensional metal oxide nanomaterials for next-generation rechargeable batteries, Adv. Mater. 29 (2017), 1700176.

[17] X.H. Cao, C.L. Tan, X. Zhang, W. Zhao, H. Zhang, Solution-processed two-dimensional metal dichalcogenide-based nanomaterials for energy storage and conversion, Adv. Mater. 28 (2016) 6167–6196.

[18] X.F. Wang, S. Kajiyama, H. Linuma, Eiji Hosono, S. Oro, I. Moriguchi, M. Okubo, A. Yamada, Pseudocapacitance of MXene nanosheets for high-power sodium-ion hybrid capacitors, Nat. Commun. 6 (2015) 6544.

[19] Y. Han, T.Q. Li, Y. Li, J. Tian, Z. Yi, N. Lin, Y.T. Qian, Stabilizing antimony nanocrystals within ultrathin carbon nanosheets for high-performance K-ion storage, Energy Storage Mater. 20 (2019) 46–54.

[20] B. Sun, X.D. Huang, S.Q. Chen, P.R. Munroe, G.X. Wang, Porous graphene nanoarchitectures- an efficient catalyst for low charge-overpotential, long life and high capacity lithium-oxygen batteries, Nano Lett. 14 (2014) 3145–3152.

[21] L.C. Yin, J. Liang, G.M. Zhou, F. Li, R. Saito, H.M. Cheng, Understanding the interactions between lithium polysulfides and N-doped graphene using density functional theory calculations, Nano Energy 25 (2016) 203–210.

[22] J.H. Du, S.F. Pei, L.P. Ma, H.M. Cheng, Carbon nanotube- and graphene-based transparent conductive films for optoelectronic devices, Adv. Mater. 26 (2014) 1958–1991.

[23] Y.M. Sun, X.L. Hu, W. Luo, Y.H. Huang, Self-assembled hierarchical MoO_2/graphene nanoarchitectures and their application as a high-performance anode material for lithium-ion batteries, ACS Nano 5 (2011) 7100–7107.

[24] J.M. Huang, R.J. Meng, L.H. Zu, Z.J. Wang, N. Feng, Z.Y. Yang, Y. Yu, J.H. Yang, Sandwich-like $Na_{0.23}TiO_2$ nanobelt/Ti_3C_2 MXene composites from a scalable in situ transformation reaction for long-life high-rate lithium/sodium-ion batteries, Nano Energy 46 (2018) 20–28.

[25] Y.Q. Yang, G. Liu, J.T.S. Irvine, H.M. Cheng, Enhanced photocatalytic H_2 production in core-shell engineered rutile TiO_2, Adv. Mater. 28 (2016) 5850–5856.

[26] G. Liu, H.G. Yang, J. Pan, Y.Q. Yang, G.Q. Lu, H.M. Cheng, Titanium dioxide crystals with tailored facets, Chem. Rev. 114 (2014) 9559–9612.

[27] L.R. Hou, L. Lian, L.H. Zhang, G. Pang, C.Z. Yuan, X.G. Zhang, Self-sacrifice template fabrication of hierarchical mesoporous Bi-component-active ZnO/$ZnFe_2O_4$ sub-microcubes as superior anode towards high-performance lithium-ion battery, Adv. Funct. Mater. 25 (2015) 238–246.

[28] Y.W. Wang, L. Yu, X.W. Lou, Formation of triple-shelled molybdenum-polydopamine hollow spheres and their conversion into MoO_2/carbon composite hollow spheres for lithium-ion batteries, Angew. Chem. Int. Ed. 55 (2016) 14668–14672.

[29] Z.Y. Fan, J. Liang, W. Yu, S.J. Ding, S.D. Cheng, G. Yang, Y.L. Wang, Y.X. Xi, K. Xi, R.V. Kumar, Ultrathin NiO nanosheets anchored on a highly ordered nanostructured carbon as an enhanced anode material for lithium ion batteries, Nano Energy 16 (2015) 152–162.

[30] Y.H. Dou, J.T. Xu, B.Y. Ruan, Q.,N. Liu, Y.D. Pan, Z.Q. Sun, S.X. Dou, Atomic layer-by-layer Co_3O_4/graphene composite for high performance lithium-ion batteries, Adv. Energy Mater. 6 (2016) 1501835.

[31] P. Poizot, S. Laruelle, S. Grugeon, L. Dupont, J.M. Tarascon, Nano-sized transition-metal oxides as negative-electrode materials for lithium-ion batteries, Nature 407 (2000) 496–499.

[32] M.P. Browne, Z. Sofer, M. Pumera, Layered and two dimensional metal oxides for electrochemical energy conversion, Energy Environ. Sci. 12 (2019) 41–58.

[33] M. Chhowalla, H.S. Shin, G. Eda, L.J. Li, K.P. Loh, H. Zhang, The chemistry of two-dimensional layered transition metal dichalcogenide nanosheets, Nat. Chem. 5 (2013) 263–275.

[34] V. Nicolosi, M. Chhowalla, M.G. Kanatzidis, M.S. Strano, J.N. Coleman, Liquid exfoliation of layered materials, Science 340 (2013) 1226419.

[35] J.H. Han, M. Kwak, Y. Kim, J. Cheon, Recent advances in the solution-based preparation of two-dimensional layered transition metal chalcogenide nanostructures, Chem. Rev. 118 (2018) 6151–6188.

[36] Y.F. Dong, Z.S. Wu, S.H. Zheng, X.H. Wang, J.Q. Qin, S. Wang, X.Y. Shi, X.H. Bao, Ti_3C_2 MXene-derived sodium/potassium titanate nanoribbons for high-performance sodium/potassium ion batteries with enhanced capacities, ACS Nano 11 (2017) 4792–4800.

[37] K.H. Nam, K.J. Jeon, C.M. Park, Layered germanium phosphide-based anodes for high-performance lithium- and sodium-ion batteries, Energy Storage Mater. 17 (2019) 78–87.

[38] Y.Q. Teng, H.L. Zhao, Z.J. Zhang, Z.L. Li, Q. Xia, Y. Zhang, L.N. Zhao, X.F. Du, Z.H. Du, P.P. Lv, K. Swierczek, MoS_2 nanosheets vertically grown on graphene sheets for lithium-ion battery anodes, ACS Nano 10 (2016) 8526–8535.

[39] T. Ma, W.C. Ren, X.Y. Zhang, Z.B. Liu, Y. Gao, L.C. Yin, X.L. Ma, F. Ding, H.M. Cheng, Edge-controlled growth and kinetics of single-crystal graphene domains by chemical vapor deposition, Proc. Natl. Acad. Sci. U.S.A. 110 (2013) 20386–20391.

[40] T. Ma, Z.B. Liu, J.X. Wen, Y. Gao, X.B. Ren, H.J. Chen, C.H. Jin, X.L. Ma, N.S. Xu, H.M. Cheng, W.C. Ren, Tailoring the thermal and electrical transport properties of graphene films by grain size engineering, Nat. Commun. 8 (2017), 14486.

[41] H. Jiang, H.F. Ma, Y. Jin, L.F. Wang, F. Gao, Q.Y. Lu, Hybrid α-Fe_2O_3@$Ni(OH)_2$ nanosheet composite for highrate-performance supercapacitor electrode, Sci. Rep. 6 (2016) 31751.

[42] Y.Q. Zhu, C.B. Cao, S. Tao, W.S. Chu, Z.Y. Wu, Y.D. Li, Ultrathin nickel hydroxide and oxide nanosheets: synthesis, characterizations and excellent supercapacitor performances, Sci. Rep. 4 (2014) 5787.

[43] S. Jaśkaniec, C. Hobbs, A.S. Ascaso, J. Coelho, M.P. Browne, D. Tyndall, T. Sasaki, V. Nicolosi, Low-temperature synthesis and investigation into the formation mechanism of high quality Ni-Fe layered double hydroxides hexagonal platelets, Sci. Rep. 8 (2018) 4179.

[44] T. Zhang, X.M. Ge, Z. Zhang, N.N. Tham, Z.L. Liu, A. Fisher, J.Y. Lee, Improving the electrochemical oxygen reduction activity of manganese oxide nanosheets with sulfurization-induced nanopores, ChemCatChem 10 (2018) 422–429.

[45] L.H. Tan, J. Lv, X.R. Xu, H.F. Zhao, C.M. He, H. Wang, W.F. Zheng, Construction of MXene/NiO composites through in-situ precipitation strategy for dispersibility improvement of NiO nanoparticles, Ceram. Int. 45 (2019) 6597–6600.

[46] Y. Zhu, L.L. Peng, Z.W. Fang, C.S. Yan, X. Zhang, G.H. Yu, Structural engineering of 2D nanomaterials for energy storage and catalysis, Adv. Mater. 30 (2018), 1706347.

[47] S. Abada, G. Marlair, A. Lecocq, M. Petit, V.S. Moynot, F. Huet, Safety focused modeling of lithium-ion batteries: a review, J. Power Sources 306 (2016) 178–192.

[48] X.X. Zuo, J. Zhu, P.M. Buschbaum, Y.J. Cheng, Silicon based lithium-ion battery anodes: a chronicle perspective review, Nano Energy 31 (2017) 113–143.

[49] G.M. Zhou, F. Li, H.M. Cheng, Progress in flexible lithium batteries and future prospects, Energy Environ. Sci. 7 (2014) 1307–1338.

[50] C. Liu, F. Li, L.P. Ma, H.M. Cheng, Advanced materials for energy storage, Adv. Mater. 22 (2010) E28–E62.

[51] N. Li, Z.P. Chen, W.C. Ren, F. Li, H.M. Cheng, Flexible graphene-based lithium ion batteries with ultrafast charge and discharge rates, Proc. Natl. Acad. Sci. U.S.A. 109 (2012) 17360–17365.

[52] Y.T. Hu, Y. Wu, J. Wang, Manganese-oxide-based electrode materials for energy storage applications: how close are we to the theoretical capacitance? Adv. Mater. 30 (2018), 1802569.

[53] Y.J. Tang, S.S. Zheng, Y.X. Xu, X. Xiao, H.G. Xue, H. Pang, Advanced batteries based on manganese dioxide and its composites, Energy Storage Mater. 12 (2018) 284–309.

[54] Y.F. Deng, L.N. Wan, Y. Xie, X.S. Qin, G.H. Chen, Recent advances in Mn-based oxides as anode materials for lithium ion batteries, RSC Adv. 4 (2014) 23914–23935.

[55] P. Xiong, R.Z. Ma, N. Sakai, Takayoshi Sasaki, Genuine unilamellar metal oxide nanosheets confined in a superlattice-like structure for superior energy storage, ACS Nano 12 (2018) 1768–1777.

[56] Z.Y. Sui, C.Y. Wang, K.W. Shu, Q.S. Yang, Y. Ge, G.G. Wallace, B.H. Han, Manganese dioxide-anchored three-dimensional nitrogen-doped graphene hybrid aerogels as excellent anode materials for lithium ion batteries, J. Mater. Chem. 3 (2015) 10403–10412.

[57] Y.X. Shi, X.F. Pan, B. Li, M.M. Zhao, H. Pang, Co_3O_4 and its composites for high-performance Li-ion batteries, Chem. Eng. J. 343 (2018) 427–446.

[58] C.S. Yan, C.D. Lv, Y. Zhu, G. Chen, J.X. Sun, G.H. Yu, Engineering 2D nanofluidic Li-ion transport channels for superior electrochemical energy storage, Adv. Mater. 29 (2017), 1703909.

[59] W.X. Song, K.Y. Ji, A. Aguadero, P.R. Shearing, D.J.L. Brett, F. Xie, D.J. Riley, Co_3O_4 hollow nanospheres doped with $ZnCo_2O_4$ via thermal vapor mechanism for fast lithium storage, Energy Storage Mater. 14 (2018) 324–334.

[60] D.H. Chen, L.L. Peng, Y.F. Yuan, Y. Zhu, Z.W. Fang, C.S. Yan, G. Chen, R.S. Yassar, J. Lu, K. Amine, G.H. Yu, Two-dimensional holey Co_3O_4 nanosheets for high-rate alkali-ion batteries: from rational synthesis to in-situ probing, Nano Lett. 17 (2017) 3907–3913.

[61] Y.Y. Lu, Q. Zhao, N. Zhang, K.X. Lei, F.J. Li, J. Chen, Facile spraying synthesis and high-performance sodium storage of mesoporous MoS_2/C microspheres, Adv. Funct. Mater. 26 (2016) 911–918.

[62] Y. Fang, Y.y. Lv, R.c. Che, H.Y. Wu, X.H. Zhang, D. Gu, G.F. Zheng, D.Y. Zhao, Two-dimensional mesoporous carbon nanosheets and their derived graphene nanosheets: synthesis and efficient lithium ion storage, J. Am. Chem. Soc. 135 (2013) 1524–1530.

[63] X. Zhao, J.H. Sui, F. Li, H.T. Fang, H.E. Wang, J.Y. Li, W. Cai, G.Z. Cao, Lamellar $MoSe_2$ nanosheets embedded with MoO_2 nanoparticles: novel hybrid nanostructures promoted excellent performances for lithium ion batteries, Nanoscale 8 (2016) 17902–17910.

[64] B. Hu, L.Q. Mai, W. Chen, F. Yang, From MoO_3 nanobelts to MoO_2 nanorods: structure transformation and electrical transport, ACS Nano 3 (2009) 478–482.

[65] X. Zhao, H.E. Wang, X.X. Chen, J. Cao, Y.D. Zhao, Z.G. Nealec, W. Cai, J.H. Sui, G.Z. Cao, Tubular MoO_2 organized by 2D assemblies for fast and durable alkali-ion storage, Energy Storage Mater. 11 (2018) 161–169.

[66] N. Chen, Y. Yao, D.X. Wang, Y.J. Wei, X.F. Bie, C.Z. Wang, G. Chen, Fei Du, $LiFe(MoO_4)_2$ as a novel anode material for lithium-ion batteries, ACS Appl. Mater. Interfaces 6 (2014) 10661–10666.

[67] Y.S. Liu, C. Gao, Q. Li, H. Pang, Nickel oxide/graphene composites: synthesis and applications, Chem. Eur. Jewel. 25 (2019) 2141–2160.

[68] R.S. Kate, S.A. Khalate, R.J. Deokate, Overview of nanostructured metal oxides and pure nickel oxide (NiO) electrodes for supercapacitors: a review, J. Alloy. Comp. 734 (2018) 89–111.

[69] J. Liang, H. Hu, H. Park, C.H. Xiao, S.J. Ding, U. Paikc, X.W. Lou, Construction of hybrid bowl-like structures by anchoring NiO nanosheets on flat carbon hollow particles with enhanced lithium storage properties, Energy Environ. Sci. 8 (2015) 1707–1711.

[70] X.L. Sun, C.L. Yan, Y. Chen, W.P. Si, J.W. Deng, S. Oswald, L.F. Liu, O.G. Schmidt, Three-dimensionally "curved" NiO nanomembranes as ultrahigh rate capability anodes for Li-ion batteries with long cycle lifetimes, Adv. Energy Mater. 4 (2014), 1300912.

[71] Y. Xia, W.K. Zhang, Z. Xiao, H. Huang, H.J. Zeng, X.R. Chen, F. Chen, Y.P. Gan, X.Y. Tao, Biotemplated fabrication of hierarchically porous NiO/C composite from lotus pollen grains for lithium-ion batteries, J. Mater. Chem. 22 (2012) 9209–9215.

[72] Ha Wei, E.F. Rodriguez, A.F. Hollenkamp, A.I. Bhatt, D.H. Chen, R.A. Caruso, High reversible pseudocapacity in mesoporous yolk-shell anatase TiO_2/TiO_2(B) microspheres used as anodes for Li-ion batteries, Adv. Funct. Mater. 27 (2017), 1703270.

[73] X.J. Yan, Y.Y. Wang, C.C. Liu, M. Guo, J.Y. Tao, J. Cao, D.J. Fu, L.Y. Dai, X.W. Yang, Engineering two-dimensional pores in freestanding TiO_2/graphene gel film for high performance lithium ion battery, J. Energy Chem. 27 (2018) 176–182.

[74] H. Hu, L. Yu, X.H. Gao, Z. Lin, X.W. Lou, Hierarchical tubular structures constructed from ultrathin TiO_2(B) nanosheets for highly reversible lithium storage, Energy Environ. Sci. 8 (2015) 1480–1483.

[75] J.M. Li, W. Wan, H.H. Zhou, J.J. Li, D.S. Xu, Hydrothermal synthesis of TiO_2(B) nanowires with ultrahigh surface area and their fast charging and discharging properties in Li-ion batteries, Chem. Commun. 47 (2011) 3439–3441.

[76] X. Min, B. Sun, S. Chen, M.H. Fang, X.W. Wu, Y.G. Liu, A. Abdelkader, Z.H. Huang, T. Liu, K. Xi, R.V. Kumar, A textile-based SnO_2 ultra-flexible electrode for lithium-ion batteries, Energy Storage Mater. 16 (2019) 597–606.

[77] B. Lu, J. Lin, R.Z. Hu, H. Wang, J.W. Liu, M. Zhu, C@MoS_2@PPy sandwich-like nanotube arrays as an ultrastable and high-rate flexible anode for Li/Na-ion batteries, Energy Storage Mater. 14 (2018) 118–128.

[78] Y.Y. Wang, J.H. Zhou, J.H. Wu, F.J. Chen, P.R. Li, N. Han, W.J. Huang, Y.P. Liu, H.L. Ye, F.P. Zhao, Y.G. Li, Engineering SnS_2 nanosheet assemblies for enhanced electrochemical lithium and sodium ion storage, J. Mater. Chem. 5 (2017) 25618–25624.

[79] Z.Q. Zhu, Y.X. Tang, Z.S. Lv, J.Q. Wei, Y.Y. Zhang, R.H. Wang, W. Zhang, H.R. Xia, M.Z. Ge, X.D. Chen, Fluoroethylene carbonate enabling a robust LiF-rich solid electrolyte interphase to enhance the stability of the MoS_2 anode for lithium-ion storage, Angew. Chem. Int. Ed. 57 (2018) 3656–3660.

[80] K. Wang, H.P. Wu, Y.N. Meng, Z.X. Wei, Conducting polymer nanowire arrays for high performance supercapacitors, Small 10 (2014) 14–31.

[81] C.C. Zhang, Y. Wang, S.S. Cheng, X.T. Zhang, B.B. Fu, W.P. Hu, Assembly of π-conjugated nanosystems for electronic sensing devices, Adv. Electron. Mater. 3 (2017), 1700209.

[82] Z.Y. Zhang, S.L. Wu, J.Y. Cheng, W.J. Zhang, MoS_2 nanobelts with (002) plane edges-enriched flat surfaces for high-rate sodium and lithium storage, Energy Storage Mater. 15 (2018) 65–74.

[83] Y.J. Gong, S.B. Yang, L. Zhan, L.L. Ma, R. Vajtai, P.M. Ajayan, A bottom-up approach to build 3D architectures from nanosheets for superior lithium storage, Adv. Funct. Mater. 24 (2014) 125–130.

[84] L. Zhang, H.B. Wu, Y. Yan, X. Wang, X.W. Lou, Hierarchical MoS_2 microboxes constructed by nanosheets with enhanced electrochemical properties for lithium storage and water splitting, Energy Environ. Sci. 7 (2014) 3302–3306.

[85] F. Zhou, S. Xin, H.W. Liang, L.T. Song, S.H. Yu, Carbon nanofibers decorated with molybdenum disulfide nanosheets: synergistic lithium storage and enhanced electrochemical performance, Angew. Chem. Int. Ed. 53 (2014) 11552–11556.

[86] X. Hu, Y. Li, G. Zeng, J.C. Jia, H.B. Zhan, Z.H. Wen, Three-dimensional network architecture with hybrid nanocarbon composites supporting few-layer MoS_2 for lithium and sodium storage, ACS Nano 12 (2018) 1592–1602.

[87] B. Luo, Y. Fang, B. Wang, J.S. Zhou, H.H. Song, L.J. Zhi, Two dimensional grapheae-SnS_2 hybrids with superior rate capability for lithium ion storage, Energy Environ. Sci. 5 (2012) 5226–5230.

[88] Y.P. Du, Z.Y. Yin, X.H. Rui, Z.Y. Zeng, X.J. Wu, J.Q. Liu, Y.Y. Zhu, J.X. Zhu, X. Huang, Q.Y. Yan, H. Zhang, A facile, relative green, and inexpensive synthetic approach toward large-scale production of SnS_2 nanoplates for high-performance lithium-ion batteries, Nanoscale 5 (2013) 1456–1459.

[89] B.H. Qu, C.Z. Ma, G. Ji, C.H. Xu, J. Xu, Y.S. Meng, T.H. Wang, J.Y. Lee, Layered SnS_2-reduced graphene oxide composite-a high-capacity, high-rate, and long-cycle life sodium-ion battery anode material, Adv. Mater. 26 (2014) 3854–3859.

[90] L. Wu, J. Zheng, L. Wang, X.H. Xiong, Y.Y. Shao, G. Wang, J.H. Wang, S.K. Zhong, M.H. Wu, PPy-encapsulated SnS_2 nanosheets stabilized by defects on a TiO_2 support as a durable anode material for lithium-ion batteries, Angew. Chem. Int. Ed. 58 (2019) 811–815.

[91] C.T. Gao, L. Li, A.O. Raji, A. Kovalchuk, Z.W. Peng, H.L. Fei, Y.M. He, N.D. Kim, Q.F. Zhong, E.Q. Xie, J.M. Tour, Tin disulfide nanoplates on graphene nanoribbons for full lithium ion batteries, ACS Appl. Mater. Interfaces 7 (2015) 26549–26556.

[92] Q.B. Yun, Q.P. Lu, X. Zhang, C.L. Tan, H. Zhang, Three-dimensional architectures constructed from transition metal dichalcogenide nanomaterials for electrochemical energy storage and conversion, Angew. Chem. Int. Ed. 57 (2018) 626–646.

[93] J.H. Zhou, L. Wang, M.Y. Yang, J.H. Wu, F.J. Chen, W.J. Huang, N. Han, H.L. Ye, F.P. Zhao, Y.Y. Li, Y.G. Li, Hierarchical VS_2 nanosheet assemblies: a universal host material for the reversible storage of alkali metal ions, Adv. Mater. 29 (2017), 1702061.

[94] Y. Jing, Z. Zhou, C.R. Cabrera, Z.F. Chen, Metallic VS_2 monolayer: a promising 2D anode material for lithium ion batteries, J. Phys. Chem. C 117 (2013) 25409–25413.

[95] S. Jeong, D. Yoo, J. Jang, M. Kim, J. Cheon, Well-defined colloidal 2-D layered transition-metal chalcogenide nanocrystals via generalized synthetic protocols, J. Am. Chem. Soc. 134 (2012) 18233–18236.

[96] J.L. Zhang, C.F. Du, Z.F. Dai, W. Chen, Y. Zheng, B. Li, Y. Zong, X. Wang, J.W. Zhu, Q.Y. Yan, NbS_2 nanosheets with M/Se (M = Fe, Co, Ni) codopants for Li^+ and Na^+ storage, ACS Nano 11 (2017) 10599–10607.

[97] J. Heo, H. Jeong, Y. Cho, J. Lee, K. Lee, S. Nam, E. Lee, S. Lee, H. Lee, S.W. Hwang, S. Park, Reconfigurable van der waals hetero-structured devices with metal-insulator transition, Nano Lett. 16 (2016) 6746–6754.

[98] D. Ovchinnikov, F. Gargiulo, A. Allain, D.J. Pasquier, D. Dumcenco, C. Ho, O.V. Yazyev, A. Kis, Disorder engineering and conductivity dome in ReS_2 with electrolyte gating, Nat. Commun. 7 (2016) 12391.

[99] N.R. Pradhan, A. McCreary, D. Rhodes, Z.G. Lu, S. Feng, E. Manousakis, D. Smirnov, R. Namburu, M. Dubey, A.R.H. Walker, H. Terrones, M. Terrones, V. Dobrosavljevic, L. Balicas, Metal to insulator quantum-phase transition in few-layered ReS_2, Nano Lett. 15 (2015) 8377–8384.

[100] M.L. Mao, C.Y. Cui, M.G. Wu, M. Zhang, T. Gao, X.L. Fan, J. Chen, T.H. Wang, J.M. Ma, C.S. Wang, Flexible ReS_2 nanosheets/N-doped carbon nanofibers-based paper as a universal anode for alkali (Li, Na, K) ion battery, Nano Energy 45 (2018) 346–352.

[101] Q. Zhang, S.J. Tan, R.G. Mendes, Z.T. Sun, Y.T. Chen, X. Kong, Y.H. Xue, M.H. Rümmeli, X.J. Wu, S.L. Chen, L. Fu, Extremely weak van der waals coupling in vertical ReS_2 nanowalls for high-current-density lithium-ion batteries, Adv. Mater. 28 (2016) 2616–2623.

[102] Z. Hu, Q.N. Liu, S.L. Chou, S.X. Dou, Advances and challenges in metal sulfides/selenides for next-generation rechargeable sodium-ion batteries, Adv. Mater. 29 (2017), 1700606.

[103] K. Xu, P.Z. Chen, X.L. Li, C.Z. Wu, Y.Q. Guo, J.Y. Zhao, X.J. Wu, Y. Xie, Ultrathin nanosheets of vanadium diselenide: a metallic two-dimensional material with ferromagnetic charge-density-wave behavior, Angew. Chem. Int. Ed. 52 (2013) 10477–10481.

[104] F.W. Ming, H.F. Liang, Y.J. Lei, W.L. Zhang, H.N. Alshareef, Solution synthesis of VSe_2 nanosheets and their alkali metal ion storage performance, Nano Energy 53 (2018) 11–16.

[105] B. Anasori, M.R. Lukatskaya, Y. Gogotsi, 2D metal carbides and nitrides (MXenes) for energy storage, Nat. Rev. Mater. 2 (2017) 16098.

[106] X.H. Wu, Z.Y. Wang, M.Z. Yu, L.Y. Xiu, J.S. Qiu, Stabilizing the MXenes by carbon nanoplating for developing hierarchical nanohybrids with efficient lithium storage and hydrogen evolution capability, Adv. Mater. 29 (2017), 1607017.

[107] M. Ghidiu, M.R. Lukatskaya, M.Q. Zhao, Y. Gogotsi, M.W. Barsoum, Conductive two-dimensional titanium carbide "clay" with high volumetric capacitance, Nature 516 (2014) 78–81.

[108] Q. Tang, Z. Zhou, P.W. Shen, Are MXenes promising anode materials for Li ion batteries? Computational studies on electronic properties and Li storage capability of Ti_3C_2 and $Ti_3C_2X_2$ (X = F, OH) monolayer, J. Am. Chem. Soc. 134 (2012) 16909–16916.

[109] R.J. Meng, J.M. Huang, Y.T. Feng, L.H. Zu, C.X. Peng, L.R. Zheng, L. Zheng, Z.B. Chen, G.L. Liu, B.J. Chen, Y.L. Mi, J.H. Yang, Black phosphorus quantum dot/Ti_3C_2 MXene nanosheet composites for efficient electrochemical lithium/sodium-ion storage, Adv. Energy Mater. 8 (2018), 1801514.

[110] Y.T. Liu, P. Zhang, N. Sun, B. Anasori, Q.Z. Zhu, H. Liu, Y. Gogotsi, B. Xu, Self-assembly of transition metal oxide nanostructures on MXene nanosheets for fast and stable lithium storage, Adv. Mater. 30 (2018), 1707334.

[111] W. Ai, J. Jiang, J.H. Zhu, Z.X. Fan, Y.L. Wang, H. Zhang, W. Huang, T. Yu, Supramolecular polymerization promoted in situ fabrication of nitrogen-doped porous graphene sheets as anode materials for Li-ion batteries, Adv. Energy Mater. 5 (2015), 1500559.

[112] L. Qie, W.M. Chen, Z.H. Wang, Q.G. Shao, X. Li, L.X. Yuan, X.L. Hu, W.X. Zhang, Y.H. Huang, Nitrogen-doped porous carbon nanofiber webs as anodes for lithium ion batteries with a superhigh capacity and rate capability, Adv. Mater. 24 (2012) 2047–2050.

[113] J. Sun, H.M. Liu, X. Chen, D.G. Evans, W.S. Yang, X. Duan, Carbon nanorings and their enhanced lithium storage properties, Adv. Mater. 25 (2013) 1125–1130.

[114] W. Ai, Z.M. Luo, J. Jiang, J.H. Zhu, Z.Z. Du, Z.X. Fan, L.H. Xie, H. Zhang, W. Huang, T. Yu, Nitrogen and sulfur codoped graphene: multifunctional electrode materials for high-performance Li-ion batteries and oxygen reduction reaction, Adv. Mater. 26 (2014) 6186–6192.

[115] Y.M. Shi, H.N. Li, L. Li, Recent advances in controlled synthesis of twodimensional transition metal dichalcogenides via vapour deposition techniques, Chem. Soc. Rev. 44 (2015) 2744–2756.

[116] N. Liu, P. Kim, J.H. Kim, J.H. Ye, S. Kim, C.J. Lee, Large-area atomically thin MoS_2 nanosheets prepared using electrochemical exfoliation, ACS Nano 8 (2014) 6902–6910.

[117] C.L. Tan, H. Zhang, Wet-chemical synthesis and applications of non-layer structured two-dimensional nanomaterials, Nat. Commun. 6 (2015) 7873.

[118] Z.M. Hu, X. Xiao, H.Y. Jin, T.Q. Li, M. Chen, Z. Liang, Z.F. Guo, J. Li, J. Wan, L. Huang, Y.R. Zhang, G. Feng, J. Zhou, Rapid mass production of two-dimensional metal oxides and hydroxides via the molten salts method, Nat. Commun. 8 (2017) 15630.

[119] Z.P. Chen, W.C. Ren, L.B. Gao, B.L. Liu, S.F. Pei, H.M. Cheng, Three-dimensional flexible and conductive interconnected graphene networks grown by chemical vapour deposition, Nat. Mater. 10 (2011) 424–428.
[120] Y. Lee, X.Q. Zhang, W.J. Zhang, M.T. Chang, C.T. Lin, K.D. Chang, Y.C. Yu, J.T. Wang, C. Chang, L. Li, T. Lin, Synthesis of large-area MoS_2 atomic layers with chemical vapor deposition, Adv. Mater. 24 (2012) 2320–2325.
[121] D. Wang, W.W. Zhou, R. Zhang, J.J. Zeng, Y. Du, S. Qi, C.X. Cong, C.Y. Ding, X.X. Huang, G.W. Wen, T. Yu, Mass production of large-sized, nonlayered 2D nanosheets: their directed synthesis by a rapid "gel-blowing" strategy, and applications in Li/Na storage and catalysis, Adv. Mater. 30 (2018), 1803569.
[122] J. Mei, Y.W. Zhang, T. Liao, X.M. Peng, G.A. Ayoko, Z.Q. Sun, Black phosphorus nanosheets promoted 2D-TiO_2-2D heterostructured anode for high-performance lithium storage, Energy Storage Mater. 19 (2019) 424–431.
[123] X.M. Xu, P.J. Wu, Q. Li, W. Yang, X. Zhang, X.P. Wang, J.S. Meng, C.J. Niu, Li Q. Mai, Realizing stable lithium and sodium storage with high areal capacity using novel nanosheet-assembled compact CaV_4O_9 microflowers, Nano Energy 50 (2018) 606–614.
[124] X.Y. Yue, A. Abulikemu, X.L. Li, Q.Q. Qiu, F. Wang, X.J. Wu, Y.N. Zhou, Vermiculite derived porous silicon nanosheet as a scalable and low cost anode material for lithium-ion batteries, J. Power Sources 410 (2019) 132–136.
[125] H.X. Zhang, S.L. Jing, Y.J. Hu, H. Jiang, C.Z. Li, A flexible freestanding Si/rGO hybrid film anode for stable Li-ion batteries, J. Power Sources 307 (2016) 214–219.
[126] J. Ryu, D. Hong, S. Choi, Soojin Park, Synthesis of ultrathin Si nanosheets from natural clays for lithium-ion battery anodes, ACS Nano 10 (2016) 2843–2851.
[127] J.J. Liu, Y. Yang, P.B. Lyu, P. Nachtigall, Y.X. Xu, Few-layer silicene nanosheets with superior lithium-storage properties, Adv. Mater. 30 (2018) 1800838.
[128] Z.N. Liu, K.L. Xu, H. Sun, S.Y. Yin, One-step synthesis of single-layer MnO_2 nanosheets with multi-role sodium dodecyl sulfate for high-performance pseudocapacitors, Small 11 (2015) 2182–2191.
[129] K. Lu, Z.Y. Hu, Z.H. Xiang, J.Z. Ma, B. Song, J.T. Zhang, H.Y. Ma, Cation intercalation in manganese oxide nanosheets: effects on lithium and sodium storage, Angew. Chem. Int. Ed. 55 (2016) 10448–10452.
[130] L.B. Ma, X. Gao, W.J. Zhang, H. Yuan, Y. Hu, G.Y. Zhu, R.P. Chen, T. Chen, Z.X. Tie, J. Liu, T. Wu, Z. Jin, Ultrahigh rate capability and ultralong cycling stability of sodium-ion batteries enabled by wrinkled black titania nanosheets with abundant oxygen vacancies, Nano Energy 53 (2018) 91–96.
[131] J. Chen, W.X. Song, H.S. Hou, Y. Zhang, M.J. Jing, X.N. Jia, X.B. Ji, Ti^{3+} self-doped dark rutile TiO_2 ultrafine nanorods with durable high-rate capability for lithium-ion batteries, Adv. Funct. Mater. 25 (2015) 6793–6801.
[132] H.C. Zhang, Y. Jiang, Z.Y. Qi, X.W. Zhong, Y. Yu, Sulfur doped ultra-thin anatase TiO_2 nanosheets/graphene nanocomposite for high-performance pseudocapacitive sodium storage, Energy Storage Mater. 12 (2018) 37–43.
[133] X. Xu, B. Chen, J.P. Hu, B.W. Sun, X.H. Liang, N. Li, S.A. Yang, H. Zhang, W. Huang, Yu Ting, Heterostructured TiO_2 spheres with tunable interiors and shells toward improved packing density and pseudocapacitive sodium storage, Adv. Mater. (2019), https://doi.org/10.1002/adma.201904589.
[134] K. Wu, J. Zhan, G. Xu, C. Zhang, D.Y. Pan, M.H. Wu, MoO_3 nanosheet arrays as superior anode materials for Li- and Na-ion batteries, Nanoscale 10 (2018) 16040–16049.
[135] Q.Q. Yang, M.C. Liu, Y.M. Hu, Y. Xu, L.B. Kong, L. Kang, Facile synthesis of MoS_2/graphite intercalated composite with enhanced electrochemical performance for sodium ion battery, J. Energy Chem. 27 (2018) 1208–1213.
[136] Z. Hu, L.X. Wang, K. Zhang, J.B. Wang, F.Y. Cheng, Z.L. Tao, J. Chen, MoS_2 nanoflowers with expanded interlayers as high-performance anodes for sodium-ion batteries, Angew. Chem. Int. Ed. 53 (2014) 12794–12798.
[137] X. Xu, R.S. Zhao, W. Ai, B. Chen, H.F. Du, L.S. Wu, H. Zhang, W. Huang, T. Yu, Controllable design of MoS_2 nanosheets anchored on nitrogen-doped graphene: toward fast sodium storage by tunable pseudocapacitance, Adv. Mater. 30 (2018), 1800658.
[138] H. Kim, J.B. Cook, H. Lin, J.S. Ko, S.H. Tolbert, V. Ozolins, B. Dunn, Oxygen vacancies enhance pseudocapacitive charge storage properties of MoO_{3-x}, Nat. Mater. 16 (2017) 454.
[139] D. Sun, D.L. Ye, P. Liu, Y.G. Tang, J. Guo, L.Z. Wang, H.Y. Wang, MoS_2/graphene nanosheets from commercial bulky MoS_2 and graphite as anode materials for high rate sodium-ion batteries, Adv. Energy Mater. 8 (2018), 1702383.
[140] G. Wang, J. Zhang, S. Yang, F. Wang, X.D. Zhuang, K. Müllen, X.L. Feng, Vertically aligned MoS_2 nanosheets patterned on electrochemically exfoliated graphene for high-performance lithium and sodium storage, Adv. Energy Mater. 8 (2018), 1702254.
[141] X.H. Rui, H.T. Tan, Q.Y. Yan, Nanostructured metal sulfides for energy storage, Nanoscale 6 (2014) 9889–9924.
[142] Y.V. Lim, Y. Wang, D.Z. Kong, L. Guo, J.I. Wong, L.K. Ang, H.Y. Yang, Cubic-shaped WS_2 nanopetals on prussian blue derived nitrogen-doped carbon nanoporous framework for high performance sodiumion batteries, J. Mater. Chem. 5 (2017) 10406–10415.
[143] X.F. Zheng, H.E. Wang, C. Wang, Z. Deng, L.H. Chen, Y. Li, T. Hasan, B.L. Su, 3D interconnected macro-mesoporous electrode with self-assembled NiO nanodots for high-performance supercapacitor-like Li-ion battery, Nano Energy 22 (2016) 269–277.
[144] C.H. Yang, X. Ou, X.H. Xiong, F.H. Zheng, R.Z. Hu, Y. Chen, M.L. Liu, K. Huang, V_5S_8-graphite hybrid nanosheets as a high rate-capacity and stable anode material for sodium-ion batteries, Energy Environ. Sci. 10 (2017) 107–113.
[145] D.S. Wang, Y.Y. Zhao, R.Q. Lian, D. Yang, D. Zhang, X. Meng, Y.H. Liu, Y.J. Wei, G. Chen, Atomic insight into the structural transformation and anionic/cationic redox reactions of VS_2 nanosheets in sodium-ion batteries, J. Mater. Chem. 6 (2018) 15985–15992.
[146] T.F. Zhou, W.K. Pang, C.F. Zhang, J.P. Yang, Z.X. Chen, H.K. Liu, Z.P. Guo, Enhanced sodium-ion battery performance by structural phase transition from two-dimensional hexagonal-SnS_2 to orthorhombic-SnS, ACS Nano 8 (2014) 8323–8333.
[147] K.J. Griffith, K.M. Wiaderek, G. Cibin, L.E. Marbella, C.P. Grey, Niobium tungsten oxides for high-rate lithium-ion energy storage, Nature 559 (2018) 556–563.
[148] X. Xu, R.S. Zhao, B. Chen, L.S. Wu, C.J. Zou, W. Ai, H. Zhang, W. Huang, T. Yu, Progressively exposing active facets of 2D nanosheets toward enhanced pseudocapacitive response and high-rate sodium storage, Adv. Mater. 31 (2019), 1900526.
[149] D.L. Chao, C.G. Zhu, P.H. Yang, X.H. Xia, J.L. Liu, J. Wang, X.F. Fan, S.V. Savilov, J.Y. Lin, H.J. Fan, Z.X. Shen, Array of nanosheets render ultrafast and high-capacity Na-ion storage by tunable pseudocapacitance, Nat. Commun. 7 (2016), 12122.
[150] Q. Wu, L.F. Jiao, J. Du, J.Q. Yang, L.J. Guo, Y.C. Liu, Y.J. Wang, H.T. Yuan, One-pot synthesis of three-dimensional SnS_2 hierarchitectures as anode material for lithium-ion batteries, J. Power Sources 239 (2013) 89–93.
[151] V.L. Chevrier, G. Ceder, Challenges for Na-ion negative electrodes, J. Electrochem. Soc. 158 (2011) A1011–A1014.
[152] E. Cho, K. Song, M.H. Park, K.W. Nam, Y.M. Kang, SnS 3D flowers with superb kinetic properties for anodic use in next-generation sodium rechargeable batteries, Small 12 (2016) 2510–2517.
[153] J. Ding, H. Zhou, H.L. Zhang, T. Stephenson, Z. Li, D. Karpuzov, D. Mitlin, Exceptional energy and new insight with sodium-selenium battery based on carbon nanosheet cathode and pseudographite anode, Energy Environ. Sci. 10 (2017) 153–165.
[154] Y. Yao, M.L. Chen, R. Xu, S.F. Zeng, H. Yang, S.F. Ye, F.F. Liu, X.J. Wu, Y. Yu, CNT interwoven nitrogen and oxygen dual-doped porous carbon nanosheets as free-standing electrodes for high-performance Na-Se and K-Se flexible batteries, Adv. Mater. 30 (2018), 1805234.
[155] Y.S. Yun, Y.U. Park, S.J. Chang, B.H. Kim, J. Choi, J.J. Wang, D. Zhang, P.V. Braun, H.J. Jin, K. Kang, Crumpled graphene paper for high power sodium battery anode, Carbon 99 (2016) 658–664.
[156] Y.W. Liu, T.F. Zhou, Y. Zheng, Z.H. He, C. Xiao, W.K. Pang, W. Tong, Y.M. Zou, B.C. Pan, Z.P. Guo, Y. Xie, Local electric field facilitates high-performance Li-ion batteries, ACS Nano 11 (2017) 8519–8526.
[157] Q.H. Liang, Y. Zheng, C.F. Du, Y.B. Luo, J. Zhao, H. Ren, J.W. Xu, Q.Y. Yan, Asymmetric-layered tin thiophosphate: an emerging 2D ternary anode for high-performance sodium ion full cell, ACS Nano 12 (2018) 12902–12911.
[158] M. Naguib, V.N. Mochalin, M.W. Barsoum, Y. Gogotsi, MXenes: a new family of two-dimensional materials, Adv. Mater. 26 (2014) 992–1005.
[159] B. Anasori, Y. Xie, M. Beidaghi, J. Lu, B.C. Hosler, L. Hultman, P.R.C. Kent, Y. Gogotsi, M.W. Barsoum, Two-dimensional, ordered, double transition metals carbides (MXenes), ACS Nano 9 (2015) 9507–9516.
[160] M. Naguib, J. Halim, J. Lu, K.M. Cook, L. Hultman, Y. Gogotsi, M.W. Barsoum, New two-dimensional niobium and vanadium carbides as promising materials for Li-ion batteries, J. Am. Chem. Soc. 135 (2013) 15966–15969.
[161] X.Q. Xie, M.Q. Zhao, B. Anasori, K. Maleski, C.E. Ren, J.W. Li, B.W. Byles, E. Pomerantseva, G.X. Wang, Y. Gogotsi, Porous heterostructured MXene/carbon nanotube composite paper with high volumetric capacity for sodium-based energy storage devices, Nano Energy 26 (2016) 513–523.
[162] H. Furukawa, K.E. Cordova, M. O'Keeffe, O.M. Yaghi, The chemistry and applications of metal-organic frameworks, Science 341 (2013), 1230444.
[163] B. Li, H.M. Wen, Y.J. Cui, W. Zhou, G.D. Qian, B.L. Chen, Emerging multifunctional metal-organic framework materials, Adv. Mater. 28 (2016) 8819–8860.
[164] Z.G. Jiang, T.F. Liu, L.J. Yan, J. Liu, F.F. Dong, M. Ling, C.D. Liang, Z. Lin, Metal-organic framework nanosheets-guided uniform lithium deposition for metallic lithium batteries, Energy Storage Mater. 11 (2018) 267–273.
[165] C. Li, Q. Yang, M. Shen, J.Y. Ma, B.W. Hu, The electrochemical Na intercalation/extraction mechanism of ultrathin cobalt(II) terephthalate-based MOF nanosheets revealed by synchrotron X-ray absorption spectroscopy, Energy Storage Mater. 14 (2018) 82–89.
[166] W. Quan, Z.L. Tang, Y. Hong, T. S, Wang, Z.T. Zhang, Hydroxyl compensation effects on the cycle stability of Nickel-Cobalt layered double hydroxides synthesized via solvothermal method, Electrochim. Acta 182 (2015) 445–451.
[167] J. Zhou, J.C. Chen, M.X. Chen, J. Wang, X.Z. Liu, B. Wei, Z.C. Wang, J.J. Li, L. Gu, Q.H. Zhang, H. Wang, L. Guo, Few-layer bismuthene with anisotropic expansion for high-areal-capacity sodium-ion batteries, Adv. Mater. 31 (2019), 1807874.
[168] H. Xia, X.H. Zhu, J.Z. Liu, Q. Liu, S. Lan, Q.H. Zhang, X.Y. Liu, J.K. Seo, T.T. Chen, L. Gu, Y.S. Meng, A monoclinic polymorph of sodium birnessite for ultrafast and ultrastable sodium ion storage, Nat. Commun. 9 (2018) 5100.
[169] B.W. Lin, X.H. Zhu, L.Z. Fang, X.Y. Liu, S. Li, T. Zhai, L. Xue, Q.B. Guo, J. Xu, H. Xia, Birnessite nanosheet arrays with high K content as a high-capacity and ultrastable cathode for K-ion Batteries, Adv. Mater. 31 (2019), 1900060.
[170] J.H. Lee, H.J. Lee, S.H. Choi, J. Shin, S.Y. Chung, J.W. Choi, Superlattice formation of crystal water in layered double hydroxides for long-term and fast operation of aqueous rechargeable batteries, Adv. Energy Mater. 8 (2018), 1703572.
[171] Y.X. Huang, C.Y. Zhu, S.L. Zhang, X.M. Hu, K. Zhang, W.H. Zhou, S.Y. Guo, F. Xu, H.B. Zeng, Ultrathin bismuth nanosheets for stable Na-ion batteries: clarification of structure and phase transition by in situ observation, Nano Lett. 19 (2019) 1118–1123.
[172] Z.G. Yang, J.L. Zhang, M.C.W.K. Meyer, X.C. Lu, D. Choi, J.P. Lemmon, J. Liu, Electrochemical energy storage for green grid, Chem. Rev. 111 (2011) 3577–3613.

[173] P. Canepa, G.S. Gautam, D.C. Hannah, R. Malik, M. Liu, K.G. Gallagher, K.A. Persson, G. Ceder, Odyssey of multivalent cathode materials: open questions and future challenges, Chem. Rev. 117 (2017) 4287–4341.
[174] H. Tang, Z. Peng, L. Wu, F.Y. Xiong, C.Y. Pei, Q.Y. An, L.Q. Mai, Vanadium-based cathode materials for rechargeable multivalent batteries: challenges and opportunities, Electrochem. Energy Rev. 1 (2018) 169–199.
[175] S.J. Su, Z.G. Huang, Y.N. Li, F. Tuerxun, J. Yang, J.L. Wang, A novel rechargeable battery with a magnesium anode, a titanium dioxide cathode, and a magnesium borohydride/tetraglyme electrolyte, Chem. Commun. 51 (2015) 2641–2644.
[176] H.D. Yoo, I. Shterenberg, Y. Gofer, G. Gershinsky, N. Pour, D. Aurbach, Mg rechargeable batteries: an on-going challenge, Energy Environ. Sci. 6 (2013) 2265–2279.
[177] M.M. Huie, D.C. Bock, E.S. Takeuchi, A.C. Marschilok, K.J. Takeuchi, Cathode materials for magnesium and magnesium-ion based batteries, Coord. Chem. Rev. 287 (2015) 15–27.
[178] N. Wu, Z.Z. Yang, H.R. Yao, Y.X. Yin, L. Gu, Y.G. Guo, Improving the electrochemical performance of the $Li_4Ti_5O_{12}$ electrode in a rechargeable magnesium battery by lithium-magnesium co-intercalation, Angew. Chem. Int. Ed. 54 (2015) 5757–5761.
[179] Y. Meng, Y.Y. Zhao, D.S. Wang, D. Yang, Y. Gao, R.Q. Lian, G. Chen, Y.J. Wei, Fast Li^+ diffusion in interlayer-expanded vanadium disulfide nanosheets for Li^+/Mg^{2+} hybrid-ion batteries, J. Mater. Chem. 6 (2018) 5782–5788.
[180] Y.X. Zeng, Z.Z. Lai, Y. Han, H.Z. Zhang, S.L. Xie, X.H. Lu, Oxygen-vacancy and surface modulation of ultrathin nickel cobaltite nanosheets as a high-energy cathode for advanced Zn-ion batteries, Adv. Mater. 30 (2018), 1802396.
[181] W.W. Xu, C.L. Sun, K.N. Zhao, X. Cheng, S. Rawal, Y. Xu, Y. Wang, Defect engineering activating (boosting) zinc storage capacity of MoS_2, Energy Storage Mater. 16 (2019) 527–534.
[182] G.A. Elia, K. Marquardt, K. Hoeppner, S. Fantini, R.Y. Lin, E. Knipping, W. Peters, J.F. Drillet, S. Passerini, R. Hahn, An overview and future perspectives of aluminum batteries, Adv. Mater. 28 (2016) 7564–7579.
[183] C.J. Niu, J.S. Meng, C.H. Han, K.N. Zhao, M.Y. Yan, L.Q. Mai, VO_2 nanowires assembled into hollow microspheres for high-rate and long-life lithium batteries, Nano Lett. 14 (2014) 2873–2878.
[184] S.D. Zhang, B. Shang, J.L. Yang, W.S. Yan, S.Q. Wei, Y. Xie, From VO_2 (B) to VO_2 (A) nanobelts: first hydrothermal transformation, spectroscopic study and first principles calculation, Phys. Chem. Chem. Phys. 13 (2011) 15873–15881.
[185] T. Luo, Y.P. Liu, H.F. Su, R.C. Xiao, L.T. Huang, Q. Xiang, Y. Zhou, C.G. Chen, Nanostructured-VO_2(B): a high-capacity magnesium-ion cathode and its electrochemical reaction mechanism, Electrochim. Acta 260 (2018) 805–813.
[186] T. Zhao, G.M. Zhang, F.S. Zhou, S. Zhang, C. Deng, Toward tailorable Zn-ion textile batteries with high energy density and ultrafast capability: building high-performance textile electrode in 3D hierarchical branched design, Small 14 (2018), 1802320.
[187] W. Sun, F. Wang, S. Hou, C.Y. Yang, X.L. Fan, Z.H. Ma, T. Gao, F.D. Han, R.Z. Hu, M. Zhu, C.S. Wang, Zn/MnO_2 battery chemistry with H^+ and Zn^{2+} coinsertion, J. Am. Chem. Soc. 139 (2017) 9775–9778.
[188] N.A. Kumar, M.A. Dar, R. Gul, J.B. Baek, Graphene and molybdenum disulfide hybrids: synthesis and applications, Mater. Today 18 (2015) 286–298.
[189] C.B. Zhu, X.K. Mu, P.A. Aken, Y. Yu, J. Maier, Single-layered ultrasmall nanoplates of MoS_2 embedded in carbon nanofibers with excellent electrochemical performance for lithium and sodium storage, Angew. Chem. Int. Ed. 53 (2014) 2152–2156.
[190] X. Fan, R.R. Gaddam, N.A. Kumar, X.S. Zhao, A hybrid Mg^{2+}/Li^+ battery based on interlayer-expanded MoS_2/graphene cathode, Adv. Energy Mater. 7 (2017), 1700317.
[191] H.F. Li, C.P. Han, Y. Huang, Y. Huang, M.S. Zhu, Z.X. Pei, Q. Xue, Z.F. Wang, Z.X. Liu, Z.J. Tang, Y.K. Wang, F.Y. Kang, B.H. Li, C.Y. Zhi, An extremely safe and wearable solid-state zinc ion battery based on a hierarchical structured polymer electrolyte, Energy Environ. Sci. 11 (2018) 941–951.
[192] C.Z. Wu, X.L. Lu, L.L. Peng, K. Xu, X. Peng, J.L. Huang, G.H. Yu, Y. Xie, Two-dimensional vanadyl phosphate ultrathin nanosheets for high energy density and flexible pseudocapacitors, Nat. Commun. 4 (2013) 2431.
[193] L.M. Zhou, Q. Liu, Z.H. Zhang, K. Zhang, F.Y. Xiong, S.S. Tan, Q.Y. An, Y.M. Kang, Z. Zhou, L.Q. Mai, Interlayer-spacing-regulated $VOPO_4$ nanosheets with fast kinetics for high-capacity and durable rechargeable magnesium batteries, Adv. Mater. 30 (2018), 1801984.
[194] Y.Y. Li, F. Tang, R.J. Wang, C. Wang, J.P. Liu, A novel dual-ion hybrid supercapacitor based on $NiCo_2O_4$ nanowire cathode and MoO_2-C nanofilm anode, ACS Appl. Mater. Interfaces 8 (2016) 30232–30238.
[195] Q.W. Zhou, X.Y. Wang, Y. Liu, Y.M. He, Y.F. Gao, J.R. Liu, High rate capabilities of $NiCo_2O_4$-based hierarchical superstructures for rechargeable charge storage, J. Electrochem. Soc. 161 (2014) A1922–A1926.
[196] Z.Y. Li, J.L. Li, F.Y. Kang, 3D hierarchical AlV_3O_9 microspheres as a cathode material for rechargeable aluminum-ion batteries, Electrochim. Acta 298 (2019) 288–296.
[197] J.J. Xie, C.L. Li, Z.H. Cui, X.X. Guo, Transition-metal-free magnesium-based batteries activated by anionic insertion into fluorinated graphene nanosheets, Adv. Funct. Mater. 25 (2015) 6519–6526.
[198] P. Wang, H.S. Chen, N. Li, X.Y. Zhang, S.Q. Jiao, W.L. Song, D.N. Fang, Dense graphene papers: toward stable and recoverable Al-ion battery cathodes with high volumetric and areal energy and power density, Energy Storage Mater. 13 (2018) 103–111.
[199] Y.K. Wang, R.F. Zhang, J. Chen, H. Wu, S.Y. Lu, K. Wang, H.L. Li, C.J. Harris, K. Xi, R.V. Kumar, S.J. Ding, Enhancing catalytic activity of titanium oxide in lithium-sulfur batteries by band engineering, Adv. Energy Mater. 9 (2019), 1900953.
[200] G.P. Hao, C. Tang, E. Zhang, P.Y. Zhai, J. Yin, W.C. Zhu, Q. Zhang, S. Kaskel, Thermal exfoliation of layered metal-organic frameworks into ultrahydrophilic graphene stacks and their applications in Li-S batteries, Adv. Mater. 29 (2017), 1702829.
[201] H.T.T. Pham, Y. Kim, Y.J. Kim, J.W. Lee, M.S. Park, Robust design of dual-phasic carbon cathode for lithium-oxygen batteries, Adv. Funct. Mater. 29 (2019), 1902915.
[202] K. Adpakpang, S.M. Oh, D.A. Agyeman, X.Y. Jin, N. Jarulertwathana, I.Y. Kim, T. Sarakonsri, Y.M. Kang, S.J. Hwang, Holey 2D Nanosheets of low-valent manganese oxides with an excellent oxygen catalytic activity and a high functionality as a catalyst for Li-O_2 Batteries, Adv. Funct. Mater. 28 (2018), 1707106.
[203] L. Kong, X. Chen, B.Q. Li, H.J. Peng, J.Q. Huang, J. Xie, Q. Zhang, A bifunctional perovskite promoter for polysulfide regulation toward stable lithium-sulfur batteries, Adv. Mater. 30 (2018), 1705219.
[204] S.S. Yao, J. Cui, J.Q. Huang, Z.H. Lu, Y. Deng, W.G. Chong, J.X. Wu, M.I.U. Haq, F. Ciucci, J.K. Kim, Novel 2D Sb_2S_3 nanosheet/CNT coupling layer for exceptional polysulfide recycling performance, Adv. Energy Mater. 8 (2018), 1800710.
[205] Y. Zhong, D.L. Chao, S.J. Deng, J.Y. Zhan, R.Y. Fang, Y. Xia, Y.D. Wang, X.L. Wang, X.H. Xia, J.P. Tu, Confining sulfur in integrated composite scaffold with highly porous carbon fibers/vanadium nitride arrays for high-performance lithium-sulfur batteries, Adv. Funct. Mater. 28 (2018), 1706391.
[206] J.L. Shi, C. Tang, J.Q. Huang, W.C. Zhu, Q. Zhang, Effective exposure of nitrogen heteroatoms in 3D porous graphene framework for oxygen reduction reaction and lithium-sulfur batteries, J. Energy Chem. 27 (2018) 167–175.
[207] L. Kong, B.Q. Li, H.J. Peng, R. Zhang, J. Xie, J.Q. Huang, Q. Zhang, Porphyrin-derived graphene-based nanosheets enabling strong polysulfide chemisorption and rapid kinetics in lithium-sulfur batteries, Adv. Energy Mater. 8 (2018), 1800849.
[208] H.X. Li, S. Ma, H.Q. Cai, H.H. Zhou, Z.Y. Huang, Z.H. Hou, J.J. Wu, W.J. Yang, H.B. Yi, C.P. Fu, Y.F. Kuang, Ultra-thin Fe_3C nanosheets promote the adsorption and conversion of polysulfides in lithium-sulfur batteries, Energy Storage Mater. 18 (2019) 338–348.
[209] J. Mei, T. Liao, Z.Q. Sun, Two-dimensional metal oxide nanosheets for rechargeable batteries, J. Energy Chem. 27 (2018) 117–127.
[210] Y. Wu, Y. Yu, 2D material as anode for sodium ion batteries: recent progress and perspectives, Energy Storage Mater. 16 (2019) 323–343.